Laser and Particle Beams

cambridge.org/lpb

Wavelength dependence of laser plasma interaction related to shock ignition approach

T. Pisarczyk[1], S.Yu. Gus'kov[2,3], R. Dudzak[4,5], O. Renner[4,5], D. Batani[3,6], T. Chodukowski[1], Z. Rusiniak[1], J. Dostal[5,4], N.N. Demchenko[2], M. Rosinski[1], P. Parys[1], M. Smid[4], Ph. Korneev[2,3], E. Krousky[4,5], S. Borodziuk[1], J. Badziak[1], L. Antonelli[8], L. Gizzi[7], G. Cristoforetti[7], P. Koester[7], Y. Maheut[6], L. Volpe[7], F. Baffigi[7], T. Levato[7], J. Skala[5], A. Zaras-Szydlowska[1], J. Trela[7], D. Mancelli[6], J. Ullschmied[4], M. Pfeifer[4,5], L. Juha[4,5], M. Krus[4,5], J. Hrebicek[4,5], T. Medrik[4,5], K. Jungwirth[4], M. Krupka[5] and P. Pisarczyk[9]

[1]Institute of Plasma Physics and Laser Microfusion, 01-497 Warsaw, Poland; [2]P. N. Lebedev Physical Institute of RAS, 119991 Moscow, Russian Federation; [3]National Research Nuclear University MEPhI, 115409 Moscow, Russian Federation; [4]Institute of Physics, Czech Academy of Sciences, 182 21 Prague, Czech Republic; [5]Institute of Plasma Physics, Czech Academy of Sciences, 182 00 Prague, Czech Republic; [6]Universite Bordeaux, CNRS, CEA, CELIA, Talence, France; [7]Universita di Roma La Sapienza, Rome, Italy; [8]York Plasma Institute, University of York, York, UK and [9]Warsaw University of Technology, ICS, 00-661 Warsaw, Poland

Research Article

Cite this article: Pisarczyk T *et al* (2018). Wavelength dependence of laser plasma interaction related to shock ignition approach. *Laser and Particle Beams* **36**, 405–426. https://doi.org/10.1017/S0263034618000447

Received: 1 October 2018
Revised: 11 October 2018
Accepted: 13 October 2018

Key words:
Absorption mechanisms; fast electrons; femtosecond interferometry; inertial fusion; resonant absorption; shock ignition; shockwave

Author for correspondence:
T. Pisarczyk, Institute of Plasma Physics and Laser Microfusion, 01-497 Warsaw, Poland, E-mail: tadeusz.pisarczyk@ifpilm.pl

Abstract

This paper provides a summary of recent research connected with the shock ignition (SI) concept of the inertial confinement fusion which was carried out at PALS. In the experiments, Cu planar targets coated with a thin CH layer were used. Two-beam irradiation experiment was applied to investigate the effect of preliminary produced plasma to shock-wave generation. The 1ω or 3ω main beam with a high intensity $>10^{15}$ W/cm^2 generates shock wave, while the other 1ω beam with the intensity below 10^{14} W/cm^2 creates CH pre-plasma simulating the pre-compressed plasma related to SI. Influence of laser wavelength on absorbed energy transfer to shock wave was studied by means of femtosecond interferometry and measuring the crater volume. To characterize the hot electron and ion emission, two-dimensional (2D) K_α-imaging of Cu plasma and grid collector measurements were used. In single 1ω beam experiments energy transport by fast electrons produced by resonant absorption made a significant contribution to shock-wave pressure. However, two-beam experiments with 1ω main beam show that the pre-plasma is strongly degrading the scalelength which leads to decreasing the fast electron energy contribution to shock pressure. In both the single 3ω beam experiments and the two-beam experiments with the 3ω main beam, do not show any clear influence of fast electron transport on shock-wave pressure. The non-monotonic behavior of the scalelength at changing the laser beam focal radius in both presence and absence of pre-plasma reflects the competition of plasma motion and electron heat conduction under the conditions of one-dimensional and 2D plasma expansion at large and small focal radii, respectively.

Introduction

Iodine laser PALS provides excellent opportunities for a comparative study of the interaction of laser radiation with different wavelengths. These possibilities were used in experiments (Gus'kov *et al*., 2004, 2006) to study the effect of laser-accelerated fast electrons on the efficiency of energy transfer to a shock wave in a flat target. These investigations using Cu massive planar targets irradiated by the laser beam with different wavelengths (first and third harmonics of the iodine laser) and different intensities were carried out. As diagnostics the three-frame interferometry, in combination with the diagnostics characterizing electrons, ion emission, and the crater formation efficiency, was applied. These experiments as the very first ones have shown increasing contribution of fast electrons to energy transfer to shock wave with growing intensity and wavelength of laser radiation. To determine the role of the fast electrons in the laser energy transport to shock wave next experiments were performed with the PALS iodine laser, delivering a 300 ps duration pulse at intensities of 1–50 PW/cm^2 using the first (1315 nm) and third (438 nm) harmonics radiation (Kalinowska *et al*., 2012; Gus'kov *et al*., 2014). In these experiments massive targets of Al and Cu have been irradiated at various focal spot radii of the laser beam, R_L, to identify the mechanisms of laser absorption and to determine their influence on the absorbed energy transfer to the target. The mass of the ablated solid material as well as the fraction of the laser energy deposited in the plasma have been

CAMBRIDGE UNIVERSITY PRESS

determined by using a three-frame interferometer and by measuring the volume of the crater created on the solid surface. In order to identify the absorption mechanisms, the N_e/V_{cr} parameter has been introduced for the first time. This parameter shows how many electrons participate in creation of the crater volume unit (1 cm^3). These experiments have shown a strong influence of the wavelength and the intensity of the laser beam on the efficiency of the laser energy transfer to a massive target, independent of its material. Two-dimensional (2D) numerical simulations, including fast electron transport (Gus'kov *et al.*, 2004) as well as theoretical analysis based on an analytical model (Pisarczyk *et al.*, 2015), confirmed the experimental results and demonstrated conclusively that in the case of 1ω beam, intensities of 10–50 PW/cm^2, the dominant ablation mechanism is the heating by fast electrons generated at the resonant absorption. For the maximum laser energy of 580 J and intensity of 50 PW/cm^2, the ablative pressure reaches about 180 Mbar in spite of 2D expansion of the target corona. However, for 3ω, the ablation pressure originates from thermal electron conductivity heating, and its value of about 50 Mbar is several times lower in comparison with the 1ω case. To confirm these possibilities in the generation of the high-ablative pressure in the case of the first harmonic as well as, to identify other absorption mechanisms of the laser irradiation in the case of the third harmonic which are responsible for the laser energy transport with participation of fast electrons, the further experiments at PALS for the conditions corresponding to the shock ignition (SI) conception were carried out (Koester *et al.*, 2013; Batani *et al.*, 2014; Pisarczyk *et al.*, 2014).

In these experiments, the SI conditions were simulated by two-beam irradiation of two-layer targets, consisting of massive Cu and a 25 μm thick layer of light plastic (CH) material. The first 1ω beam with energy of 40–70 J produced pre-plasma imitating the corona of the pre-compressed inertial confinement fusion (ICF) target that is a spherical target designed for creation of inertially confined thermonuclear plasma under action of pulsed energy driver. The spike-driven shock wave was generated by the main pulse (1ω or 3ω) with the intensity of radiation in the range of 1–50 PW/cm^2. In the paper of Pisarczyk *et al.* (2014), the influence of pre-plasma on parameters of the shock wave was determined from the crater volume measurements and from the electron density distribution measured by three-frame interferometry. The ignited shock wave was generated by the main pulse with energy of 200 J (either at 1ω or 3ω). The 1ω pulse with the energy of 50 J produced pre-plasma, imitating the corona of the pre-compressed ICF target. Similarly in the paper of Pisarczyk *et al.* (2015), experiments with a single 1ω beam confirmed the enhanced efficiency of energy transfer to shock wave associated with fast electrons transporting energy to the dense plasma region. However, two-beam experiments have shown a significantly decreasing efficiency of the 1ω radiation energy transmission to the solid part of the target in comparison with the case without pre-plasma. The presence of pre-plasma creates poor conditions for resonant absorption and, therefore, for the laser energy conversion to fast electrons. The significantly smaller effectiveness of the energy transfer to the shock wave is clearly seen on both the crater volumes and the density gradient data. However, these experiments have not provided data indicating alteration of the fast electron generation due to resonant absorption by any other mechanism connected with parametric plasma instabilities in the pre-plasma.

Investigations of the fast electron generation connected with parametric plasma instabilities and their influence on the generation of a strong shock wave are presented in Koester *et al.* (2013). Similarly in the previous PALS experiments (Pisarczyk *et al.*, 2014) pre-plasma was created by the 1ω auxiliary beam with an intensity about 10^{13} W/cm^2 which was achieved by enlarging the focal spot diameter to 900 μm. A strong shock was generated by the 3ω laser beam at intensities in the range of 10^{15}–10^{16} W/cm^2 at various delays with respect to the first beam. As main diagnostics X-ray spectroscopy and calorimetry of the backscattered radiation were applied. The fast electron production is characterized through 2D imaging of the K_α emission. Information on the shock pressure is obtained using shock breakout chronometry and measurements of the craters produced by the shock in a massive target. The preliminary results show a low level of backscattered radiation (<10%) mainly due to simulated Brillouin scattering. The conversion efficiency into kinetic energy of suprathermal electrons was inferred to be well below 1% and the experimental results indicate that the suprathermal electrons are predominantly generated through the simulated Raman scattering process. The mean energy of the suprathermal electron population was estimated to be ≈50 keV. The shock pressure inferred from our measurements is in the range of 60–100 Mbar for the highest laser intensities. To know better development of the parametric plasma instabilities additional two-beam experiments were carried out at PALS (Batani *et al.*, 2014). In these experiments different kinds of targets were used. To estimate the average energy of fast electrons, Cu massive targets with plastic layers of different thicknesses in front of the Cu layer were used. To allow X-ray spectroscopic measurements, the parylene (C_8H_7Cl) plastic layer with Cl was applied. To measure the velocity of shock wave by shock chronometry, two-layer targets with 25 μm plastic (parylene-C) on the laser side, and 25 μm Al (with an additional 10 μm Al step) on the rear, were used. The targets were illuminated with the 1ω auxiliary beam delivering 30 J, and the 3ω main beam delivering up to 250 J, with a delay of up to 1.2 ns with respect to the auxiliary beam. As in previous experiments, the auxiliary beam was focused with an intensity of 10^{13} W/cm^2 in an extended focal spot diameter to create an approximately one-dimensional (1D) plasma. To produce uniform irradiation the beam was smoothed with a random phase plate. These investigations confirmed that using the third harmonic of the PALS laser as a main beam, one can generate a strong shock with the ablative pressure reaching 90 Mbar. It should be noted that it is indeed the highest pressure measured so far in this kind of experiment, showing a clear progress in approaching a SI relevant regime. Higher pressures (up to 180 Mbar) are inferred when a much larger focal spot is used.

In hitherto studies performed at PALS (described above) connected with the SI concept, the three-frame interferometry was applied. This diagnostic system worked with the second or third harmonic of the iodine laser featuring approximately 350 ps pulse, identical by its duration to the main plasma-generating laser pulse. With such relation between the diagnostic and the main laser pulse duration, this system could not allow for detailed-enough plasma probing taking into account the expansion velocities of the order of 10^8 cm/s corresponding to the fast component of the ablation plasma generated in the initial stage of the plasma expansion. Under such conditions blurring of interference fringes close to the critical density region, caused by plasma movement and/or oscillations, did not allow for measurement of the maximal reachable concentration given by the wavelength of the diagnostic laser.

From the point of view of the "shock ignition" research, particularly interesting is the initial phase of the expansion related to the interaction of the laser pulse with plasma generated by

https://doi.org/10.1017/S0263034618000447 Published online by Cambridge University Press

the rising parts of the laser pulse itself. In this phase the above-mentioned processes of anomalous absorption appear which are responsible for the generation of fast electrons, and there are electric and magnetic fields created. They result both from the motion of electrons and the effects of various phenomena and processes occurring in the non-homogeneous plasma, such as spontaneous magnetic fields associated with the effect of crossed gradients of temperature and electron concentration. These fields can significantly modify the plasma parameters and fast transport of electrons from their source to the ablation zone (surface) and influence the formation of the shock-wave ablation pressure.

It should be emphasized that the studies of the early phase of the expansion of the ablation plasma (including the interaction of the laser pulse with the plasma produced by it) have not been the subject of detailed research so far, because it requires the use of very high resolution time diagnostics. A multi-frame interferometric system irradiated by the use of a Ti:Sa femtosecond laser with a pulse duration of about 40 fs turned out to be particularly useful diagnostics in these studies. Due to the application of the femtosecond interferometry in the research on SI carried out on PALS, for the first time information about the time changes of the electron density distributions in ablative plasma during the laser pulse interaction with plasma created by it was obtained. The space–time electron density distributions allowed determining such parameters of the ablation plasma as: the axial density profile, the scalelength, the maximal density gradient, the linear density, and the total electron number in different expansion times in the ablative plasma. Information obtained from femtosecond interferometry in combination with parameters of the electron and ion emission obtained by means of the spectroscopic measurements in the X-ray range and the grid collectors, they proved to be extremely useful from the point of view of identification of absorption mechanisms of the laser irradiation by the ablative plasma, and which are responsible for the energy transport to the shock wave, in particular of the energy carried by fast electrons.

This paper is summary of the last investigations performed in experiments at PALS related to the SI concept of the ICF (Pisarczyk *et al.*, 2015, 2016) in which comprehensive measurements involving the multi-frame femtosecond interferometry as the main diagnostic were carried out.

This paper is structured as follows. In Section "Experimental setup", the experimental setup is presented which includes description and operation of the three-frame interferometer as well as the way of synchronization of the Ti:Sa diagnostic laser with the PALS iodine laser. Results of the interferometric and the crater volume measurements with use of both 1ω and 3ω of the PALS laser to create the igniting shockwave are presented in Section "Ablation and energy transfer to shock wave". The N/V_{cr} parameter (defined in Gus'kov *et al.*, 2014; Pisarczyk *et al.*, 2014) was determined to identify of the possible absorption mechanisms of the laser radiation for different wavelengths that generate a shockwave and to assess their influence on the energy transport to the shock wave under conditions without pre-plasma as well as with pre-plasma simulating the SI concept. In Section "Fast electron emission", measurements characterizing the electron and ion emission are presented. Obtained quantitative information about the population and the energy of the fast electrons from the 2D imaging of the K_α emission, clearly demonstrate the differences between 1ω and 3ω which were used for creation of a shockwave, both without pre-plasma and with pre-plasma presence. The influence of pre-plasma for various irradiation conditions is shown on the angular distributions of ions obtained with the use of the grid collectors. Section "Ion emission measurements" concerns the results of 2D numerical simulations (2DSs). Summary of the obtained results is presented in Section "2D numerical modeling of laser–plasma interaction in different wavelength experiments".

Experimental setup

The experiments were performed using the double planar targets, Figure 1a, consisting of a massive Cu plate coated with a thin CH layer, which was irradiated by the 1ω or 3ω PALS laser beam at the energy of 250 J.

To imitate the SI conditions, the lower-intensity auxiliary 1ω beam with the energy of 40 J and angle of incidence $\alpha = 25°$ created CH-pre-plasma that was irradiated by the main beam with a delay of 1.2 ns, thus generating the shock wave in the massive part of the target. Both beams were equipped with phase plates to generate homogeneous irradiation of the target surface. As the fundamental option of measurements, two-beam experiments for different irradiation conditions of the targets depending on the focal spot radius were realized. The investigations were carried out at different intensities of the main 1ω and 3ω beams controlled by varying the focal spot radius in a range of 50–200 μm and keeping the laser energy fixed. To better characterize of the pre-plasma influence on the laser energy transport to the massive part of the target and the fast electron emission parameters, the results of two-beam experiments have been compared with the single-beam experiments (without pre-plasma) for the same irradiation condition as in the case of two-beam experiments when the pre-plasma was created.

The multiframe interferometric investigations of the ablative plasma with the femtosecond resolution and the measurements of the crater creation efficiency were the main source of information about absorption mechanisms responsible for the laser energy transport process to the shock wave generated in the solid target.

The optical scheme of the three-frame interferometric system which was used in measurements is presented in Figure 2. The optical delay line is an integral part of this system and it enables space–time separation of the diagnostic beam into three independent channels.

Transmission of mirrors in the delay line is selected in such a way to ensure the same intensity for each channel of the interferometer. The construction of the delay line enables to change the time distance between frames in the range of 0.3–3 ns. Moreover, the diagnostic beam that irradiates this line is synchronized in such a manner that the first frame is recorded in a required moment of the plasma expansion (related to the maximum intensity of the laser beam which creates the plasma). Each interferometric channel is equipped with its own independent interferometer of the folding-wave type (Kasperczuk *et al.*, 1993; Borodziuk *et al.*, 2005) and with a charge-coupled device camera (RM-4200GE) enabling registration of interferograms with the high-spatial resolution (2048×2048 pixels with a size of 7.3 μm) and the 12-bit dynamics. Cameras are connected to a computer through a Gigabit Ethernet interface and controlled by a custom-build application PALS Vision GigEV, which is capable of pre-treatment of images (modification of the Fourier spectra, correction of histograms, correction of colors, calibration, etc.). In the case of high-quality interferograms, electron density distribution may be obtained after the laser shot with on-the-fly mode. For more detailed analysis of interferograms, specialized software (created at IPPLM) is used.

https://doi.org/10.1017/S0263034618000447 Published online by Cambridge University Press

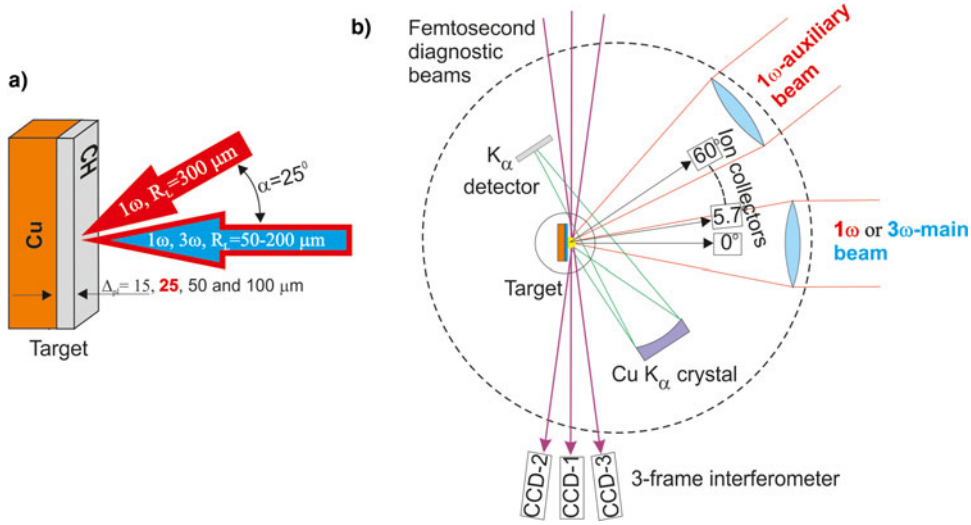

Fig. 1. Experimental set-up: (a) the construction and the geometry of irradiation of the two-layer target and (b) the location of the diagnostics on the PALS experiment.

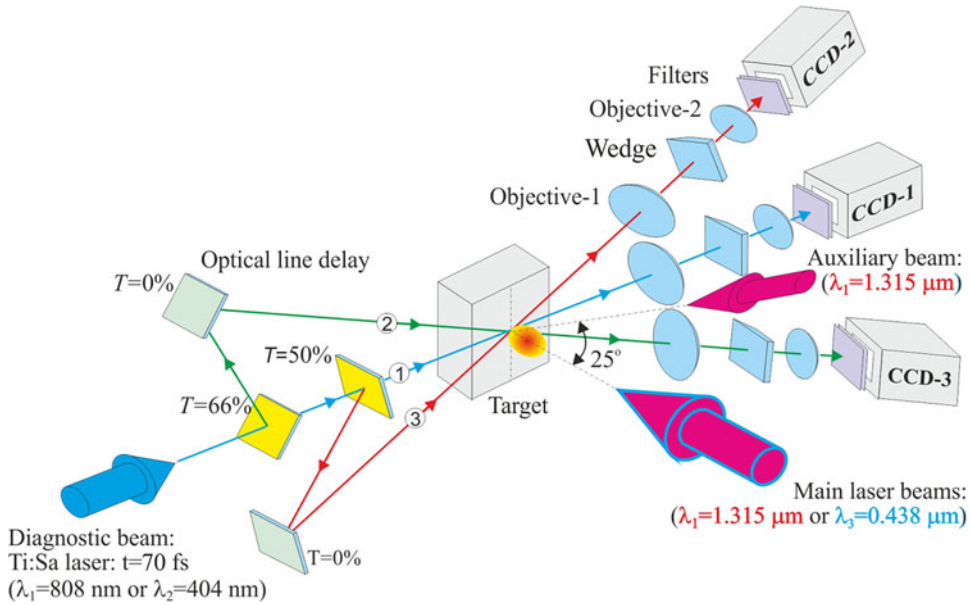

Fig. 2. Three-frame interferometric system.

To implement this three-frame interferometric system for the plasma investigation in the femtosecond regime, the method of the electronic synchronization between the Ti:Sa and the PALS laser described in Dostal *et al.* (2017) has been developed. This method enables plasma probing in selected times of plasma expansion (related to the maximum intensity of the main pulse) with the accuracy of ±100 ps.

To characterize the fast electron and ion emission, measurements were carried out using the following diagnostic sets:

- 2D imaging of the emission of Cu K_α line using spectrograph with a spherical crystal type (211) to determine the distribution of fast electron population and their energy; for this purpose experiments with use of two-layer targets, covered by the polyethylene layers of different thickness: $\Delta_{pl} = 15$, 25, 50, and 100 μm were carried out and
- the grid collectors to measure the angular distributions of the ion emission, as a source of information about the ablative plasma electron temperature, the average energy of fast electrons and the geometry of the ablative plasma expansion.

The location of the all diagnostics used in the PALS experiment is shown in Figure 1b.

Ablation and energy transfer to shock wave

Interferometric measurements. 1ω-experiments

The main aim of the femtosecond interferometry was obtaining interferograms with a high-time resolution, to observe temporal changes of the electron density distributions during the laser pulse interaction with a target. These electron density distributions are necessary to obtain information about the changes of

https://doi.org/10.1017/S0263034618000447 Published online by Cambridge University Press

the maximal density gradient and the density scalelength which are very important from the point of view of identification of the absorption mechanism, because they are responsible for the laser energy transport to the shock wave generated in the massive part of the two-layer target.

Therefore, to know the electron density of the ablative plasma in the period which included the main pulse interaction with a target, three-frames were recorded successively with the time distance of 400 ps and the first frame was recorded before the main laser pulse in the range of −400 to 200 ps relative to the maximum intensity of the main laser beam. Tens of interferograms were obtained for different conditions of irradiation of two-layer targets. Only interferograms obtained under the same conditions were analyzed.

On the basis of electron density distributions, the maximum density gradient and the density scalelength have been calculated. To obtain the information about these parameters, an exponential fitting of the experimental axial density profiles has been applied: $n_e(z) = n_0 e^{-z/L}$ (Pisarczyk *et al.*, 2014). The parameters of this function determine the maximum electron density gradient in the opacity zone: $(dn_e/dz)_{z=0} = -n_0/L$, where L is the density scalelength and n_0 is the maximum electron density. The time sequences of interferograms obtained for different expansion times during the interaction of the main laser pulse with the double target and at different irradiation conditions by changing the dimensions of the focal spot radius on the target were analyzed. The comparison of the electron density distributions of the ablative plasma and axial density profiles and the scalelength corresponding to these distributions obtained in the absence of the pre-plasma at different focal spot radii and for different times of the plasma stream expansion is presented in Figure 3. The time delays of each individual frame relate to the maximal intensity of the main pulse. As it results from Figure 3, the electron density distributions demonstrate the quasi-spherical character of the expansion for the small focal spot radius with the characteristic minimum of the density on the axis. When increasing the focal spot radius of the laser beam, the plasma stream expansion becomes more axial. It is seen from both the time sequence of the density distributions and the axial profiles related to larger focal spot radii: $R_L = 150$ and 200 μm. This change in the character of the ablative plasma expansion (from spherical to axial) by the relevant scalelengths is demonstrated.

The comparison of the electron density distributions of the ablative plasma and axial density profiles as well as the scalelength corresponding to these distributions obtained in the pre-plasma presence at different focal spot radii and for different times of the plasma stream expansion is presented in Figure 4.

The electron density distributions indicate that the light plasma with a higher pressure, being generated from the thin plastic layer by an auxiliary beam, limits the radial expansion of the central plasma created by the main laser beam. The radial limitation favors the axial character of the plasma expansion particularly in the case of larger focal spot radii. The radial limitation results in the growth of the electron density on the axis and in the increase of the scalelength. This is clearly demonstrated by the axial density profiles and the scalelength values in Figure 4.

In contrast, when the pre-plasma is not created, the density scalelength of the ablative plasma is considerably greater. A detailed comparison of the ablative plasma expansion in the case of absence and presence of the pre-plasma is presented in Figure 5. This figure shows the maximal density gradient, the scalelength, and the maximal density for three characteristic times of the expansion: 0, 300, and 600 ps related to the maximum intensity of the main laser beam. Single values corresponding to the chosen expansion times have been determined by approximating the experimental data.

Figure 5a shows that in the case of without the pre-plasma, the density gradient increases with the decreasing R_L for the focal spot radii smaller than 150 μm. The largest growth of the density gradient corresponds to the maximum laser pulse intensity ($t = 0$). The density gradient achieves a value of about $1 \times 10^{22}/cm^4$ for the minimum focal spot radius ($R_L = 50$ μm) and this gradient corresponds to the minimal density scalelength $L = 160$ μm. It can be explained by the fact that for the time of the ablative plasma expansion $t = 0$, the favorable conditions for high energy fast electron generation due to resonant absorption occur. This effect is responsible for the energy transfer to the shock wave generated in a solid target. As follows from Figure 5a, the density gradient also increases with increasing the focal spot radii above 150 μm. However, this growth is connected with a transition to predominating 1D expansion of the ablative plasma at large focal spot radii (Gus'kov *et al.*, 2014).

In the case of pre-plasma presence (Fig. 5b), the density gradient falls in the whole range of the focal spot radii and the expansion time includes the maximum intensity of the laser pulse and ensuing 600 ps. The scalelength is increased by approximately two times as compared with the case of with the pre-plasma absence. At the maximum laser intensity $t = 0$ and the minimal focal spot radius $R_L = 50$ μm, the scalelength grows to a level of about $L =$ 330 μm. This proves that in the presence of the pre-plasma, the effect of energy transfer by fast electrons becomes smaller. The presence of the extended pre-plasma leads to decreasing density gradients of the plasma created by the action of the main beam.

Crater volume measurements. 1ω-experiments

The crater volume and the interferometric measurements are very useful combination and they can provide essential information about mechanisms of the laser radiation absorption using the ratio N/V_{cr}, where N is the total electron number in the plasma plume, and V_{cr} is the crater volume in cm^3. This parameter defines how many numbers of thermal electrons are participating in the creation of a crater volume unit (1 cm^3). To obtain information about the N/V_{cr} parameter, the craters and interferograms obtained for the same irradiation conditions of two-layer targets were taken into account. Data about the total electron number obtained from the interferometric measurements (presented in the previous paragraph) in Figure 6 are shown. The time changes of the total number of electrons for different focal spot radii in the case of pre-plasma absence are shown in Figure 6a, while Figure 6b shows the time changes in the case of the presence of pre-plasma. As it results from the presented dependences in figures below, the total number of electrons increases during the laser pulse interaction with target, both in the cases of the absence and presence of the pre-plasma. As expected, in the case of two-beam irradiation (with pre-plasma) the total number of electrons is larger than the single-beam irradiation (without pre-plasma) and it increases with increasing of the focal spot radius.

The examples of photographs of the crater replicas and their shapes in mutually perpendicular cross-sections obtained in the case of the absence and presence of the pre-plasma for the same irradiation conditions as for the interferograms are presented in Figure 7. For measuring the crater volume the method described in the paper of Pisarczyk *et al.* (2014) was applied.

https://doi.org/10.1017/S0263034618000447 Published online by Cambridge University Press

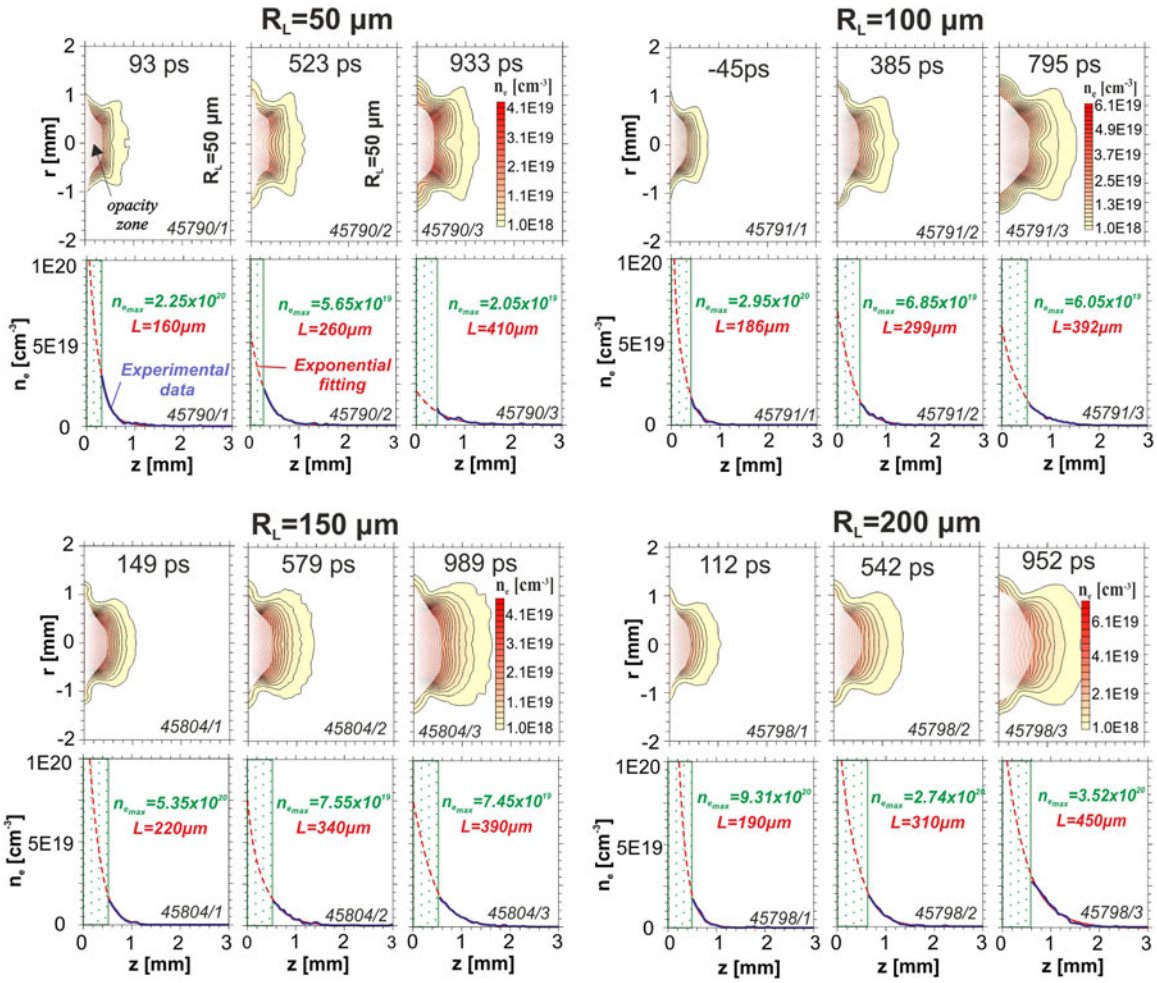

Fig. 3. Electron density distributions illustrating the time evolution of the ablative plasma expansion during the laser pulse interaction with the target at different focal spot radii in the pre-plasma absence.

Considering that the time of the crater formation is longer than the duration of the laser pulse, the N/V_{cr} parameter was evaluated only for the expansion time $t = 600$ ps, that is after the end of the main laser pulse, when both the ablation process and the processes related to absorption of laser radiation have ended. Figure 8 presents a comparison of N/V_{cr} parameter, the crater volume V_{cr}, total number of electrons N, and obtained for the target irradiation without and with the pre-plasma.

As it results from Figure 8, in the case of pre-plasma absence, the crater volumes and the N/V_{cr} parameter demonstrate the increased efficiency of the crater creation with the decreasing focal spot radius in the range of $R_L < 150$ μm. According to our previous papers (Gus'kov *et al.*, 2014; Pisarczyk *et al.*, 2014), this corresponds directly to the energy transfer into the target by fast electrons generated due to resonant absorption. However, the crater creation efficiency also grows in the range of the focal spot radii larger than $R_L = 150$ μm. When the beam radius exceeds this value, the fast electron temperature decreases (with decreasing the laser intensity) and the role of the fast electron energy transfer in the ablation process becomes smaller than the role of thermal conductivity. In this case, the crater volume growth is due to decreasing the transverse expansion of the laser-produced plasma. This is confirmed by interferometric results, which show an increasing density gradient (see Fig. 5a), that is connected with the axial (1D) expansion of the ablative plasma, which predominates in the case of the 1ω radiation and $R_L >$ 150 μm. Therefore, the transverse plasma expansion decreases, the pressure increases and hence, the efficiency of the energy transformation to the shock wave also increases. According to Borodziuk *et al.* (2004a, b) the largest crater in the massive Cu target is created by means of the 1ω laser beam focused on the focal spot radius about 300 μm.

At the pre-plasma presence, Figure 8b, the crater volume decreases to the level about 3×10^{-5} cm^3, and this value does not depend on the focal spot radius of the main laser beam. A comparison with Fig. 8a indicates that in the presence of pre-plasma, the effect of the fast electron energy transfer on the solid target is suppressed. The experimental data stating the rate of the electron number growth in the presence of pre-plasma (Fig. 8) are approximately by a factor of 1.5 larger in comparison with the case of pre-plasma absence. It can be explained by the fact that in this case the absorption coefficient (according to results of numerical simulation presented below) is two times higher than that in the case of pre-plasma absence. The rate of 8×10^{25} electrons per s can provide the number of electrons equal to approximately 1.2×10^{16} and 3.6×10^{16}. These values are about two times smaller than the data of Fig. 8, which is ascribed to the contribution of the electrons from the pre-plasma.

https://doi.org/10.1017/S0263034618000447 Published online by Cambridge University Press

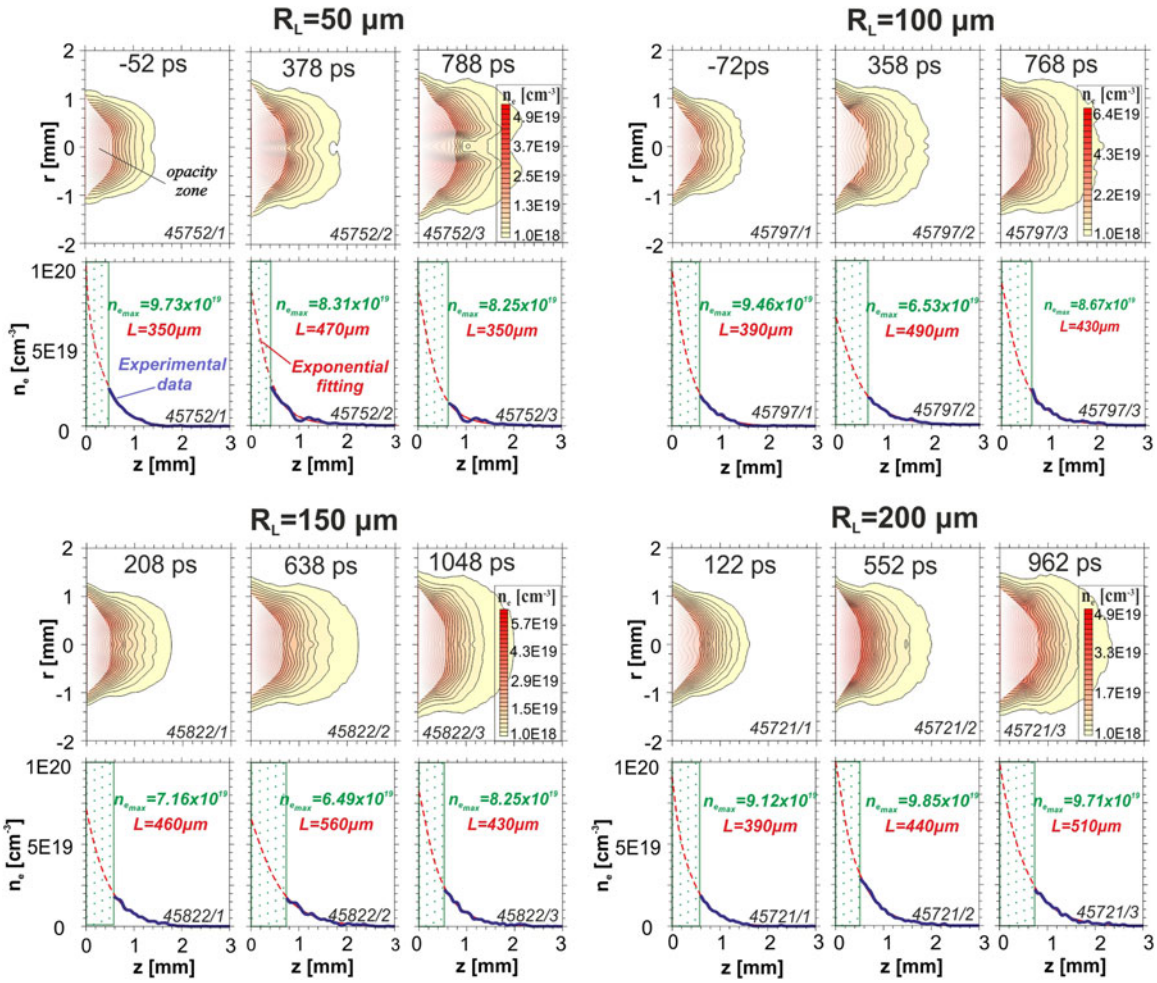

Fig. 4. Electron density distributions illustrating the time evolution of the ablative plasma expansion during the laser pulse interaction with the target at different focal spot radii in the presence pre-plasma.

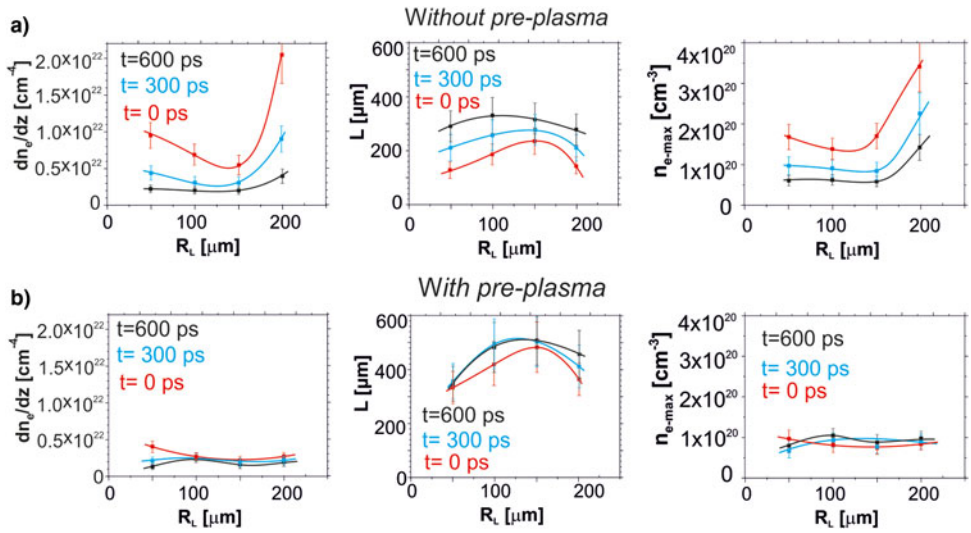

Fig. 5. Comparison of the maximal density gradient, the scalelength, and the maximal density obtained in the cases of absence and presence of the pre-plasma.

To conclude, according to the temporary changes of the gradient determined from interferometric measurements the temporal changes of the N/V_{cr} parameter confirm that electrons produced in time $t = 0$ provide the largest contribution to the creation of the craters, corresponding to the maximum of the main laser pulse intensity.

https://doi.org/10.1017/S0263034618000447 Published online by Cambridge University Press

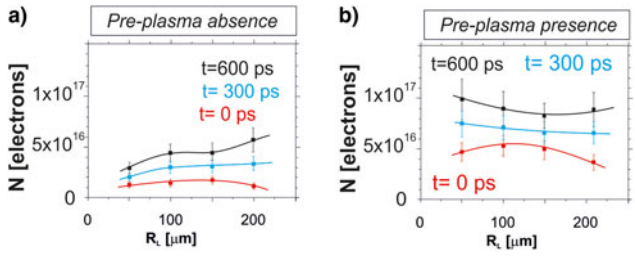

Fig. 6. Comparison of the changes of total number of electrons in the cases of absence (a) and presence of the pre-plasma (b) for three characteristic times of the expansion.

Interferometric measurements. 3ω-experiments

To simulate the SI conditions the third harmonic ($\lambda_3 = 438$ nm) iodine laser beam with the intensity of radiation in the range of 1–20 PW/cm^2 corresponding to changes of parameter $I\lambda_3^2$ of 2×10^{14}–4×10^{15} Wm^2/cm^2. The desired intensity of the main beam has been achieved at a constant laser energy at the level of about 200 J by changing the focal spot radius of the laser beam impinging the target in range of $R_L = 50$–200 μm. As in the experiments with the first harmonic of the iodine laser, to simulate the SI conditions two-beam irradiation of two-layer targets (Fig. 1) consisting of a planar massive part with Cu, covered by a 25 μm layer of polyethylene was applied. The pre-plasma, which simulates the pre-compressed plasma in a real inertial fusion experiment, was created by means of the first harmonic laser beam with an energy of about 40 J, defocused to the focal spot radius $R_L = 300$ μm. Analogously as in the 1ω-experiment, the main 3ω pulse was delayed by 1.2 ns relative to the pulse creating the pre-plasma. Obtaining information about the temporal changes of the density scalelength (L) and the maximal density gradient (dn_e/dz) on the basis of the space–time electron density distributions was the main aim of investigations using the femtosecond interferometry.

The summary comparison of the electron density distributions and the axial density profiles of the ablative plasma obtained in the absence of pre-plasma at different focal spot radii and for different times of the plasma stream expansion is presented in Figure 9. The time delay of each individual frame relates to the maximal intensity of the main pulse. On each individual frame the information about the maximal electron density in near of the target and the scalelength using by the exponential fitting the axial density profiles is given.

As results from the temporal changes of the electron density distributions and the axial density profiles, the axial expansion increases with increasing the focal spot radius and leads to an increase in the electron density on the axis at later times of the laser pulse interaction with a target. It is in contrast to temporal changes of electron density in the case of the 1ω-experiments, where the electron density on the axis decreases with the expansion time due to the spherical expansion. Consequently, a larger electron density on the axis in the vicinity of the target for the 3ω case leads to a decrease of the scalelength due to the greater axial expansion of the ablation plasma. This scalelength is on the level of $L = 200$ μm and it is almost two times smaller compared with the scalelength in the case of the 1ω-experiments.

The comparison of temporal sequences of electron density distributions of the ablative plasma obtained in the presence of pre-plasma at different focal spot radii is presented in Figure 10. As it results from Figure 10, both the equidensity lines of electron density and the space density profiles demonstrate that the light plasma with a higher pressure, being generated from a thin plastic layer by the auxiliary beam, limits radial expansion of the central plasma created by the main laser beam. The radial limitation favors the axial character of the plasma expansion particularly in the case of larger focal spot radii. These changes in the character of the ablative plasma expansion, caused both by the increasing focal spot radius and the radial expansion limitation by pre-plasma, lead to an increase in the electron density on the axis and to the elongation of the plasma stream at later times of its expansion. However, despite the increase in the electron density on the axis, the strong elongation of the plasma stream causes an increase of the scalelength. As it results from Figure 10, in the case of pre-plasma presence the scalelength is about two times larger than that when the pre-plasma is not created.

The detailed comparison of the ablative plasma expansion in the cases of absence and presence of pre-plasma is presented in Figure 11. This figure shows the maximal density gradient, the scalelength, and the maximal density for three characteristic times of expansion: 0, 300, and 600 ps in relation to the maximum intensity of the main laser beam. Single values corresponding to chosen expansion times have been determined by interpolation of the experimental data.

From Figure 11a it results that in the case of without pre-plasma the highest density gradient values correspond to the maximum laser pulse intensity ($t = 0$). Its maximum value is about 5×10^{22}/cm^4 for the focal spot radius R_L equal to 100 μm and it corresponds to the minimal scalelength $L = 100$ μm.

Such value of the scalelength is approximately the same in the whole range of the changes of the focal spot radius. For later times of plasma expansion, the density gradient decreases rapidly, reaching a value five times smaller (at $t = 600$ ps) in comparison with the maximum value, while the scalelength increases to a value about 300 μm at the same expansion time of the ablative plasma.

An increase of the focal spot radius above $R_L = 100$ μm leads to a decrease of the density gradient and to small changes in the scalelength. Further increasing the focal spot radius (above $R_L =$ 150 μm) increases the density gradient, reducing the scalelength a little, which is the result of the increasing role of 1D expansion of the ablative plasma for larger focal spot radii (Gus'kov *et al.*, 2014; Pisarczyk *et al.*, 2015).

However, the presence of pre-plasma, Figure 11b, degenerates neither the maximal density gradient nor the scalelength of electron density, unlike the case of the first harmonics main beam generating igniting shock wave (Pisarczyk *et al.*, 2015). As it results from Figure 11b, the strong limitation of the radial expansion of the 3ω ablative plasma by the external light plastic pre-plasma which is created by means of the 1ω auxiliary laser beam, leads to an increase in the electron density on the axis, and, consequently to an increase in the density gradient. The largest density gradient occurs during the intensity peak of the main laser beam ($t = 0$), for the smallest focal spot radius ($R_L = 50$ μm) and its value is about 7×10^{22}/cm^4, which is even a bit higher than in the absence of pre-plasma. However, this gradient drops rapidly, both as a function of the expansion time and focal spot radius. It should be noted also that the plasma stream formed in the presence of pre-plasma is characterized by a greater scalelength than in its absence. As it results from Fig. 11b, the smallest density scalelength, $L = 220$ μm, corresponds to the maximum laser pulse intensity ($t = 0$) and minimal focal spot radius. With the increase in the focal spot radius, the scalelength increases

https://doi.org/10.1017/S0263034618000447 Published online by Cambridge University Press

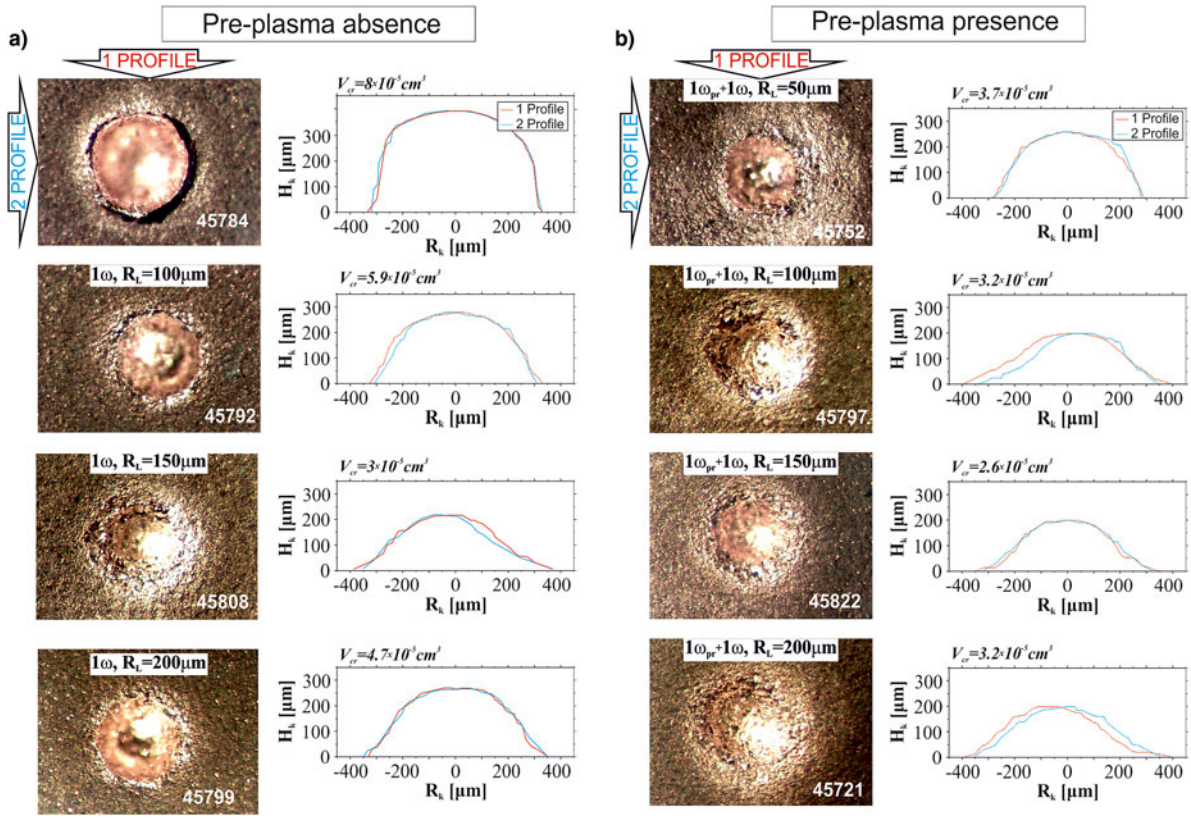

Fig. 7. The craters and their shapes in two cross-sections for different focal spot radii obtained in cases absence (a) and presence (b) of the pre-plasma.

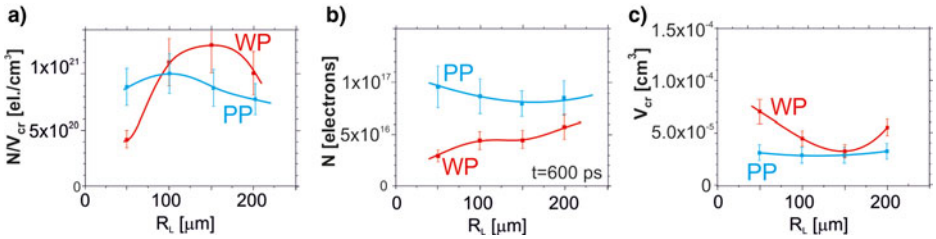

Fig. 8. Comparison of: (a) N/V_{cr} parameter, (b) the crater volumes, and (c) the total electron number obtained in the case of absence (WP) and presence (PP) of the pre-plasma.

monotonously, reaching a value of one and a half time greater (about $L = 340$ μm) than in the case of without pre-plasma. For later times of ablative plasma expansion the changes of scalelength as a function of focal spot radius are very similar to those for the initial phase of expansion. This proves the stabilizing influence of the pre-plasma on the central plasma created by the main 3ω beam.

In previous experiments carried out with the first harmonic main pulse (Pisarczyk *et al.*, 2015), a significant effect of energy transfer by fast electrons on the formation of plasma density and temperature distributions was found and, as a result, also on the formation of ablation pressure and laser energy transfer to shock wave. In the absence of pre-plasma the fast electron energy transport deep into the corona at a high-laser intensity (at small radii of laser beam) was more effective than the electron thermal conductivity and led to a significant increase in the ablation density in comparison with the low critical plasma density corresponding to the first harmonic radiation. This explains the measured rather high values of electron density gradient of about $10^{22}/\text{cm}^4$ at the small beam radii. The generation of fast electrons is due to a significant contribution of resonant mechanism of laser light absorption. The presence of pre-plasma significantly worsened both the conditions for generation of fast electrons and the effectiveness of the energy transfer by them, that was manifested by a significant decrease (two to four times) of the density gradient.

The results of the experiments with the third harmonic main pulse, presented here, do not reveal the influence of energy transfer by fast electrons on the plasma formation. The non-monotonic dependence of the density gradient on the laser beam focal spot radius in both the presence and absence of pre-plasma is determined by the competition of the processes of plasma motion and electron heat conduction under the conditions of 1D and 2D expansion at large and small values of the focal spot radius, respectively. The significant increase in the density gradient in the case of the third harmonic main pulse in comparison with the first harmonic one is due to the ninefold excess of the critical plasma density.

Crater volume measurements. 3ω-experiments

The N/V_{cr} parameter has been determined taking into account the total electron number obtained from the interferometric

https://doi.org/10.1017/S0263034618000447 Published online by Cambridge University Press

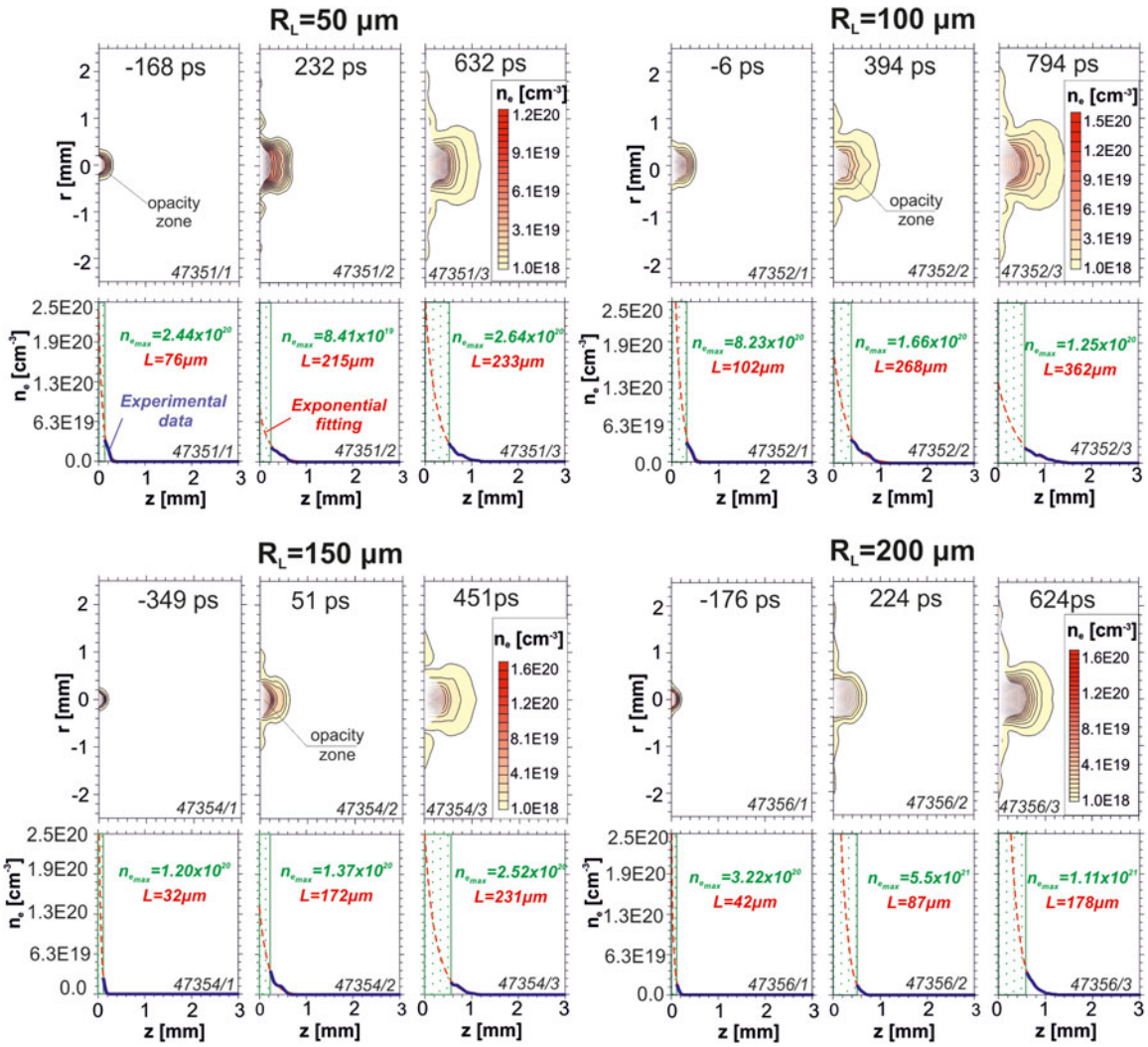

Fig. 9. Electron density distributions illustrating the time evolution of the ablative plasma expansion during the laser pulse interaction with the target at different focal spot radii in the pre-plasma absence.

measurements and the crate volume values obtained for the same experimental conditions for which interferograms were registered. A comparison of temporal changes of the total electron number in the case of absence and presence of pre-plasma is presented in Figure 12. As it follows from Figure 12, the total electron number in the plasma streams increases both with the expansion time and the focal spot radii. For measuring the volume of craters which were obtained together with interferometry, a digital microscope (HIROX-KH-8700 model) from the Institute of Optoelectronics of Military University of Technology (MUT) was used. This microscope enables determination of the crater parameters in the selected cross-sections with micron accuracy and their visualization.

The N/V_{cr} parameter was evaluated only for the expansion time $t = 600$ ps, that is after the end of the main laser pulse, when both the ablation process and processes related to absorption of laser radiation were completed. The results of calculations of the N/V_{cr} parameter, the total electron number N, and the crater volumes V_{cr}, for the different options of irradiation of two-layer targets are shown in Figure 13.

First of all, it should be noted that in comparison with the results of 1ω main pulse experiments (Pisarczyk *et al.*, 2015), in the 3ω case the crater volume increases significantly less with decreasing radius in the region of its low value, $R_L < 100$ μm. This indicates that in the case of the 3ω radiation the strong effect of energy transfer by fast electrons deep into a dense plasma, observed in the case of the 1ω case, is absent. As a result, at 3ω only one transport mechanism works, namely that caused by the electron thermal conductivity. This fact leads to just a weak growth in the crater volume with increasing laser intensity with decreasing beam radius. Furthermore, the crater volume in the case of the third harmonic main pulse is six to eight times larger in comparison with the case of the 1ω main pulse. This is due to a more efficient energy transfer to shock waves due to a larger ablation pressure associated with a significantly (ninefold) higher critical plasma density in the case of the third harmonic radiation. The presence of pre-plasma, which increases the corona mass and therefore the number of electrons N, slightly reduces the crater volume by reducing the efficiency of energy transfer by electron conductivity. At the same time, the decrease in the ratio N/V_{cr} in the case of both the absence and presence of pre-plasma

https://doi.org/10.1017/S0263034618000447 Published online by Cambridge University Press

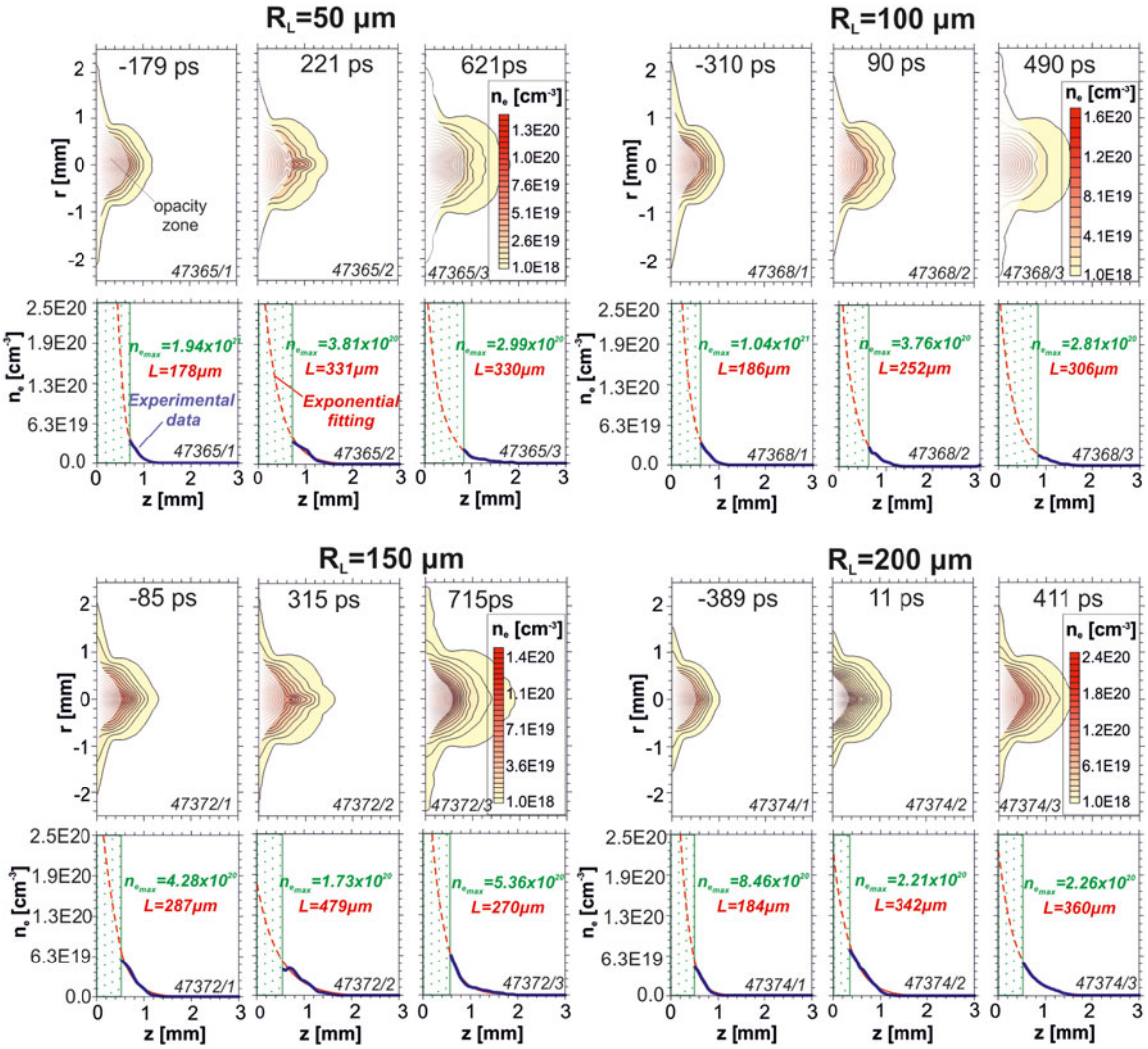

Fig. 10. Electron density distributions illustrating the time evolution of the ablative plasma expansion during the laser pulse interaction with the target at different focal spot radii in the pre-plasma presence.

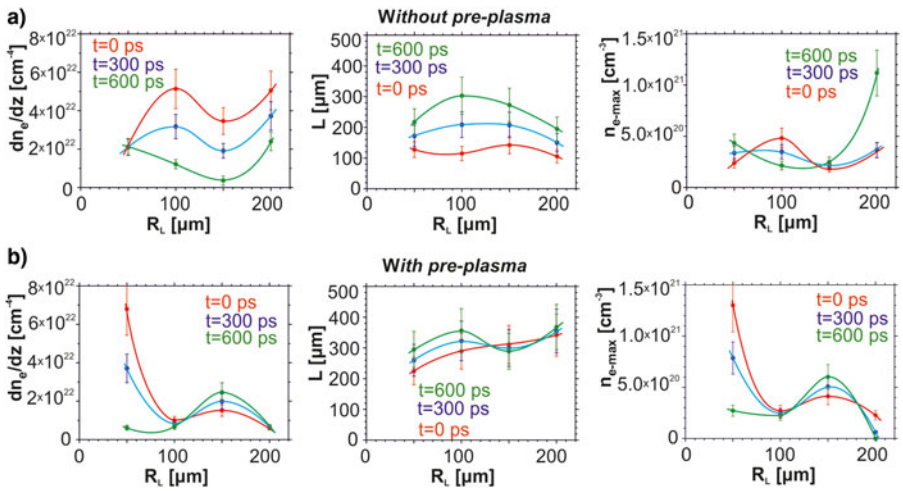

Fig. 11. Comparison of the maximal density gradient, the scalelength, and the maximal density obtained in the cases of absence and presence of the pre-plasma.

shows that in the absence of fast electron energy transfer, when the electron conductivity is the dominant mechanism of energy transfer, the most favorable conditions for the energy transfer to shock wave correspond to the plane expansion of plasma at large values of the beam radius (Gus'kov *et al.*, 2014; Pisarczyk *et al.*, 2014).

https://doi.org/10.1017/S0263034618000447 Published online by Cambridge University Press

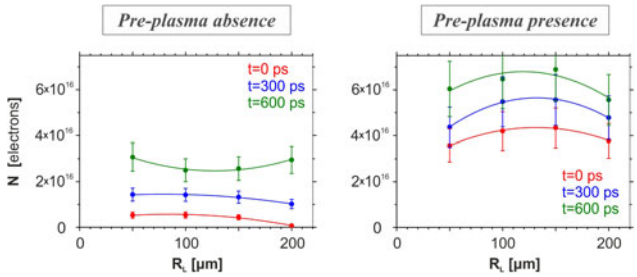

Fig. 12. Comparison of the changes of the total electron number in the cases of absence and presence of pre-plasma for three characteristic times of plasma expansion.

Fast electron emission

K_α-emission. 1ω-experiments

To characterize in more detail the impact of the pre-plasma on the laser energy transport and the formation of ablation pressure, the interferometry and crater volume measurements were complemented by measurements of the fast electron emission. The collected data were used to determine the population and energy of hot electrons (HE), as well as the conversion efficiency of the laser energy into HE for different irradiation conditions of the two-layer target is shown in Figure 1. The X-ray images were recorded using a spherically-bent crystal of quartz (422), Figure 14, which was setup as an imaging mode monochromator (with the Bragg angle $\theta_B = 88.2°$ and magnification of c/a = 1.73) to provide a distribution of the 2D-spatially resolved Cu K_α emission along the target surface (Smid *et al.*, 2013; Pisarczyk *et al.*, 2015; Renner *et al.*, 2016).

The time-integrated K_α signals attenuated by transmission through filters consisting of 10 μm of Cu, 20 μm of Al, and 40 μm of mylar were obtained with the Kodak AA400 X-ray film. The recorded images were digitized with a calibrated table-top scanner, recalculated to optical densities and to intensities of the impinging radiation by using the characteristic curve of the film.

The research was carried out using the 1ω main laser beam with the energy at the level of 250 J. The intensities of the radiation impinging onto the target were varied by changing the laser energy or the focal spot radius in range of $R_L = 50$–200 μm. To determine the energy of the fast electrons, the two-layer targets with different thicknesses of the plastic ($\Delta_{pl} = 15$; 25; 50; and 100 μm) have been used. Typical images obtained when focusing the variable energy laser beam on focal spots with radii $R_L = 50$ and 100 μm are presented in Figure 15. As is obvious from Figure 15, the intensity of the K_α signal increases with the decreasing focal spot size and with the increasing energy of the laser beam.

The 2D-resolved records contain information on the emitting area and intensity of the K_α emission generated in cold copper material by fast electrons. The quantitative evaluation of this data was based on assumption of the Maxwellian energy distribution of supra-thermal electrons impacting on the double layer target and an exponential decay of the photon emission I with the increasing thickness x of the plastic layer $I(x) = A \times \exp(-x/L)$, where L is an attenuation coefficient. The experimental data were interpreted by using Monte Carlo simulations of the electron and photon transport performed with the PENELOPE code (Salvat *et al.*, 2009). Assuming characteristic temperature T_{HE} of Maxwellian HE distribution, the trajectories of electrons propagating into the target were calculated both in the plastic and Cu layers, the generation of K_α emission inside the Cu layer and its propagation and absorption in the target was taken into account. A set of simulations was performed for different T_{HE} values and various plastic thicknesses. Each simulation calculated the probability $dp/d\Omega(\Psi)$ that one electron produces a K_α photon escaping the target in a unit solid angle at the given polar angle Ψ. These probabilities were further used in interpretation of the experimental data and in derivation of the sought interaction characteristics, for example, the exponential attenuation of the fast-electron-generated photon emission due to different-thickness surface plastic layers. The calculated dependence of the attenuation coefficient L on the supra-thermal electron energy is shown in Figure 16. The final experimental results were obtained *via* fitting the photon fluxes spatially integrated over 2D-resolved images with simulations. To determine the energy of fast electrons E, the Cu K_α emission was measured at targets with different thickness plastic layers. Results of these measurements are presented in Figure 17 showing the dependence of the detected photon fluxes on the thickness of the surface plastic layer Δ_{pl} in the absence and presence of the pre-plasma.

All the data were taken when irradiating the target by the 1ω beam focused on the focal spot with a radius of $R_L = 50$ μm. In addition to the useful K_α signal and the film noise, the recorded images captured a non-negligible amount of the continuum radiation emitted primarily by the plastic layer covering the Cu substrate. This radiation has independently been measured using self-supporting plastic foils and subtracted from the recorded images, but the uncertainty estimate has significantly increased due to the fluctuation of the background signal.

Consequently, the shown error bars indicate mainly uncertainties in the background subtraction. The number of incident photons refers to photon fluxes impinging on the filmpack, that is, when processing the recorded images, the signal attenuation in filters covering the film was taken into account. The dependences plotted in Figure 17 demonstrate the decrease of the Cu K_α photon fluxes with the increasing thickness of plastic. The best-fit values of the attenuation coefficient L and the HE energy E are also indicated in Figure 17. The fitted scalelength is about $L = 30$ μm without the pre-pulse and $L = 29$ μm for the case of the plasma presence. The simulations show that for scalelengths $L < 50$ μm, the relation is very close to T_{HE} (keV) $\approx L$ (μm). Thus we can state that the energies of the fast electrons for 1ω for both cases with and without pre-pulse are close each to other and about $T_{HE} = 29$ keV.

The effect of the pre-plasma on the total number of detected Cu K_α photons in dependence on the laser intensity, that is, on the focal spot radius, is shown in Figure 18. All these data fitted with the second degree polynomial were measured at Cu targets coated with 25 μm of plastic. As it results from Figure 18 in the case of the pre-plasma presence, the K_α emission decreases strongly with R_L. The interferometric and spectroscopic measurements seem to confirm that the presence of the pre-plasma reduces the contribution of fast electrons in the energy transfer process to the Cu massive target.

To estimate the conversion of the laser energy into fast electrons, the number of detected photons N_{K_α} was related to the number of HEs N_{HE} propagating through the target using the expression:

$$N_{HE} = \frac{N_{PH}}{(4\pi r dp/d\Omega)} \quad (1)$$

https://doi.org/10.1017/S0263034618000447 Published online by Cambridge University Press

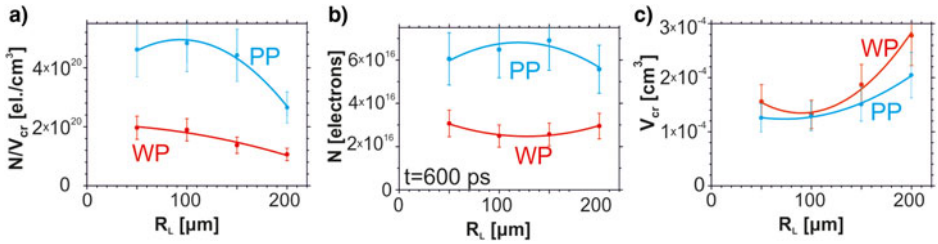

Fig. 13. Comparison of the crater volumes V_{cr} and N/V_{cr} parameter obtained in the cases of absence and presence of pre-plasma.

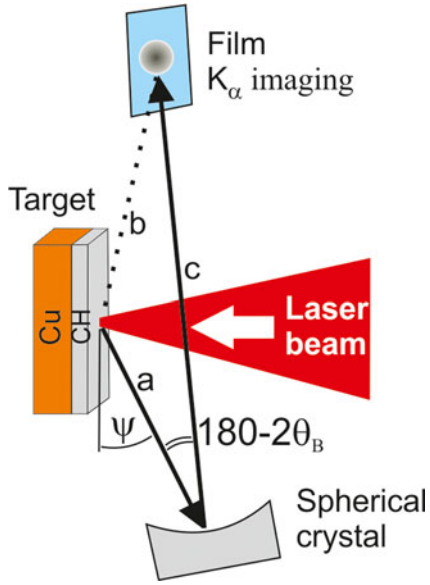

Fig. 14. The scheme of the measurement of Cu K_α emission.

where $r = 8.3 \times 10^{-7}$ is the ray tracing constant relating the fraction of photons impinging on the detector to the number of photons isotropically emitted from the cold copper into the full solid angle 4π within the Cu K_α1,2 profile (Smid *et al.*, 2013). This assumption is well justified for copper targets coated with 25 μm of plastic where the frequency shifted satellite emission generated by fast electrons in the heated copper can be neglected. By taking into account the average energies E presented in Figure 17, the found values of N_{HE} were further related to the conversion efficiency η of the laser energy into HEs. In the current experiment, the typical numbers of fast electrons N_{HE} propagating through the target were within the range of $1–5 \times 10^{12}$. The conversion efficiencies calculated as the ratio of the total energy carried by fast electrons entering the target to the energy of the main 1ω laser beam in the presence/absence of pre-plasma are shown in Figure 19.

K_α-emission. 3ω-experiments

Analogously to experiments using the 1ω main laser beam, similar studies were performed to determine the characteristics of fast electrons under irradiation of two-layer targets by the 3ω laser beam. The main aim of these measurements was to investigate the influence of the plasma formation on the fast electron generation in the presence and absence of the pre-plasma.

The experiment was carried out with the laser energy of about 200 J and various intensities resulting from changes of the focal spot radius of laser beam on the target in the range of $R_L = 50–200$ μm. To determine the energy of fast electrons, two-layer targets with different thicknesses of the plastic ($\Delta_{pl} = 15$, 25, 50, and 100 μm) were again used.

The imaging setup was the same as in the previous section "K_α-emission. 1ω-experiments" (Fig. 14). The time-integrated K_α signals attenuated by transmission through filters consisting of 10 μm of Cu, 20 μm of Al, and 40 μm of mylar were obtained with the Kodak AA400 X-ray film. The recorded images were digitized with a calibrated table-top scanner. Then the experimental data were interpreted by using the methodology presented in the previous section.

The results of the measurements showing the effect of the pre-plasma on the total number of photons detected as a function of the thickness of the surface plastic layer Δ_{pl} in the absence and presence of the pre-plasma are shown in Figure 20.

This figure demonstrates attenuation of the Cu K_α photon fluxes with the increasing thickness of the plastic and a significant increase of the emission in the presence of the pre-plasma. The best-fit values of the attenuation coefficient L and the HE energy E are also indicated in Figure 20. The characteristic energy of fast electrons produced in the case of the single-beam irradiation of the targets equals to 37 keV, while in the pre-plasma presence the value of E is almost two times higher.

The effect of the pre-plasma on the total number of the detected Cu K_α photons in dependence on the laser intensity, that is, on the focal spot radius, is shown in Figure 21.

All these data fitted with the second degree polynomial were measured using Cu targets coated with 25 μm of plastic. While the number of detected Cu K_α photons (and consequently also the production of HEs) increases only slightly with the focal spot radius in the pre-plasma absence, the presence of the pre-plasma results in a distinct growth of the fast electron population peaking at $R_L \approx 150$ μm. Obviously the increased scalelength of the ablative plasma in the presence of the pre-plasma increases both the production and the energy of fast electrons.

To estimate the conversion of the laser energy into fast electrons, the number of detected K_α photons was related to the number of HEs N_{HE} propagating through the target using expression (1). By taking into account the average energies E presented in Figure 20, the found values of N_{HE} were further related to the conversion efficiency η of the laser energy into HEs. As in the case of the 1ω-experiments (see previous section), the typical numbers of fast electrons N_{HE} propagating through the target were within the range of $1–5 \times 10^{12}$.

The conversion efficiencies calculated as the ratio of the total energy carried by fast electrons entering the target to the energy of the main 3ω laser beam in the presence/absence of pre-plasma are shown in Figure 22. The conversion efficiencies are grouped near four laser intensities 1×10^{16}, 2.5×10^{15}, 1×10^{15}, and 6×10^{14} W/cm^2 corresponding to focal spot radii of 50, 100, 150, and 200 μm, respectively. The found values of η are considerably scattered and do not display any distinct dependence on the laser

https://doi.org/10.1017/S0263034618000447 Published online by Cambridge University Press

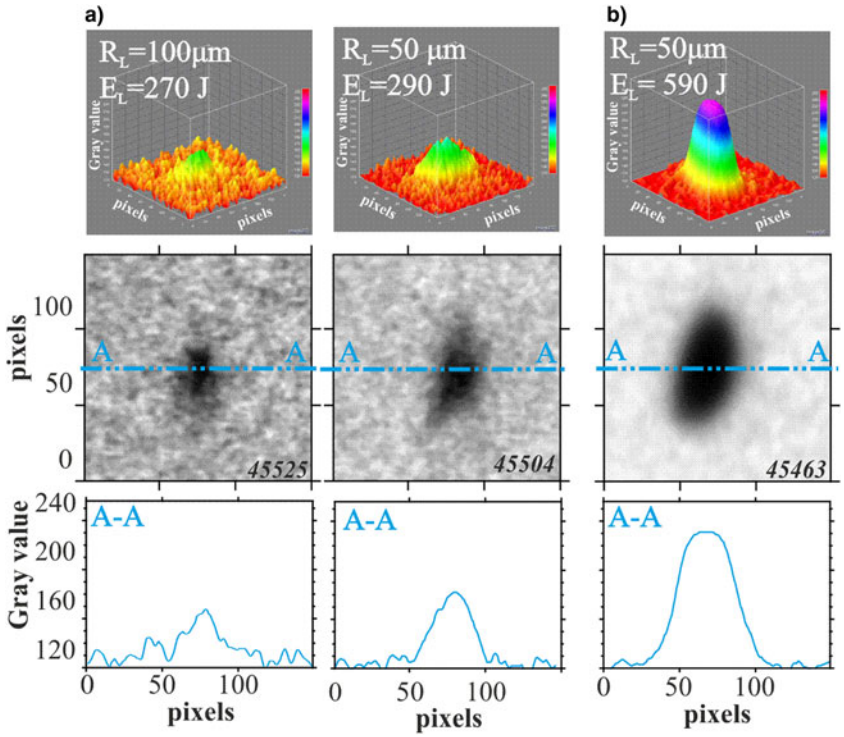

Fig. 15. Images of the K_α obtained in the case of without pre-plasma at the minimal focal spot radii for different laser energies: (a) 290 J and (b) 590 J.

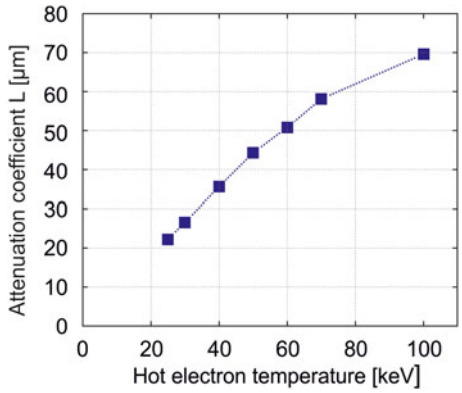

Fig. 16. Dependences of the attenuation coefficient L as a function of fast electron energy.

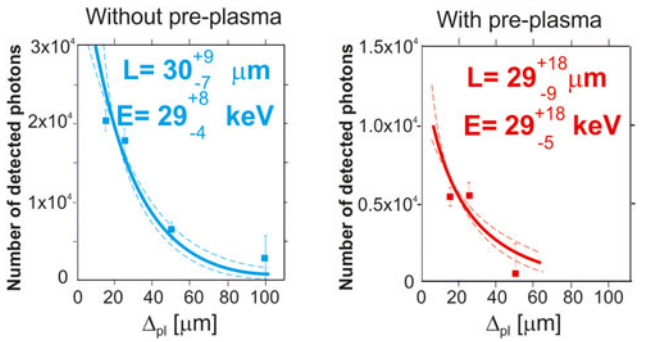

Fig. 17. Dependences of the K_α on thickness of plastic for the cases of absence and presence of the pre-plasma.

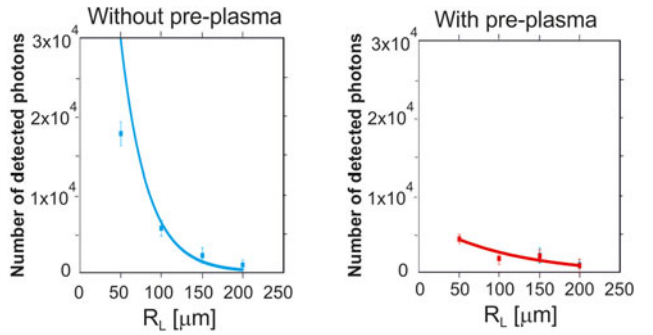

Fig. 18. The influence of pre-plasma presence on the total population of photons depending on the focal spot radius of the laser beam.

intensity. On the other hand, the presence of pre-plasma increases their average values (1.2×10^{-4} in the pre-plasma absence and 3.5×10^{-4} in its presence) by a factor of approximately 2.9.

Under given conditions of the target irradiation, the observed laser energy conversion to fast electrons is rather small in both cases of the pre-plasma presence and absence. This conversion efficiency is too small for fast electrons to provide major impact on the laser-produced plasma evolution as well as on the processes of the laser energy deposition and pressure formation in experiments using the 3ω main pulse.

Ion emission measurements

Ion emission. 1ω-experiments

The ion diagnostics applied in the PALS experiment consisted of the ion collectors which were installed at different angles (from 0 to 60°) at the distance of 40 cm from the target. The collected ion current was emitted from the two-layer targets (see Fig. 1a). The sorted oscillograms illustrating temporary changes of the ion-

https://doi.org/10.1017/S0263034618000447 Published online by Cambridge University Press

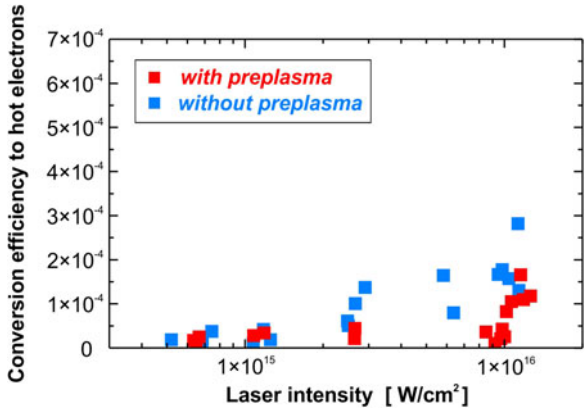

Fig. 19. Conversion efficiency of the energy of 1ω main laser beam into the total energy carried by fast electrons as a function of the laser beam intensity.

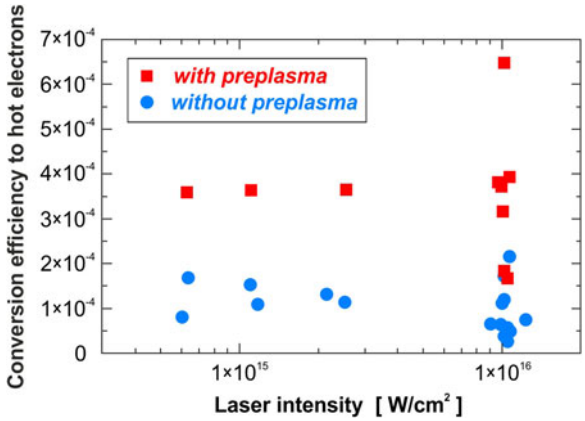

Fig. 22. Conversion efficiency of the 3ω main laser beam energy in the total energy carried by fast electrons as a function of laser beam intensity.

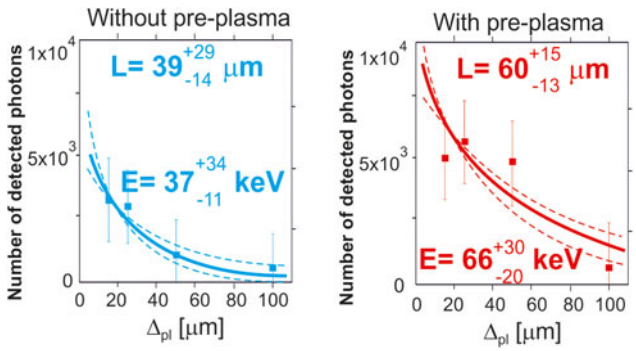

Fig. 20. Results of the 2D fast electron emission imaging showing the influence of the pre-plasma on the total population of photons, depending on the plastic layer thickness in the two-layer target in the cases of absence and presence of pre-plasma.

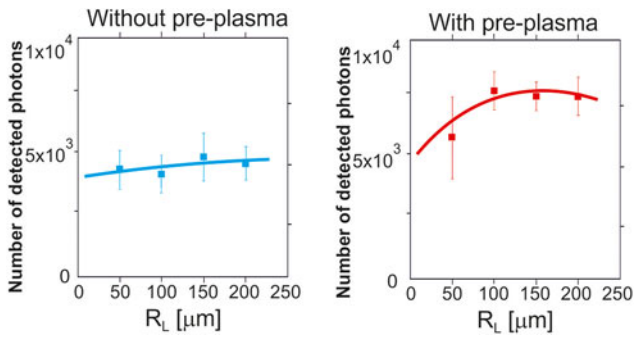

Fig. 21. Results of 2D fast electron emission imaging, showing the influence of pre-plasma on the total population of photons depending on the focal spot radius of laser beam under the conditions of absence and presence of pre-plasma.

collector signals provided by this diagnostic system are presented in Figure 23a. In the left column there are results obtained without the application of the pre-pulse and in the right column the results obtained with the pre-pulse application. The basic difference in the subsequent experimental series is in the focal radius which ranged from 50 to 200 μm. The parameters of the laser beam were at the same level for all experimental series (about 250 J in the main beam and about 40 J in the pre-pulse). The diagrams show the time dependence of the ion-collector signals as a function of time for different angles and focal diameters. The main conclusions following from these results may be summarized as below:

- The number of thermal ions (the second-delayed peak) in the case of pre-plasma presence is two to three times larger than that observed in the case of pre-plasma absence for all the beam radii. It means that the absorption coefficient in the case of pre-plasma presence is two to three times larger than in the case of pre-plasma absence. This conclusion is confirmed by the results of 2DSs presented in the next section.
- In the case of pre-plasma presence, fast ions (the first peak) are generated at all radii of the laser beam. Since the fast ions are generated in the field of fast electrons, this means that in the presence of pre-plasma also the fast electrons are generated at all laser beam radii. This conclusion agrees with the results of 2DSs predicting high efficiency of resonant absorption of laser radiation for all the radii of laser beam in the presence of pre-plasma.
- In the case of pre-plasma absence, fast ions are generated only at the radii of 100 and 50 μm. It is in agreement with the results on fast electrons generation from interferometric and X-ray spectroscopic measurements presented above.
- The time of the second peak equals to about 0.7 μs; it is approximately the same for the cases both with and without pre-plasma and for all radii of the laser beam.
- The time of the first peak (0.15 μs) is significantly shorter than that of the second peak which indicates that the energies of fast ions are much higher than those of thermal ions.

The ion-collector data not sorted according to the ion types give a possibility to determine only the scales of temperature of the plasma plume and average energy of fast electrons. Taking the time of the second peak as 0.7 μs, the average velocity of thermal ions as $(3T/2m_p)^{1/2}$ (in the $A/Z = 2$ approximation) and the distance between the target and collector equals to 40 cm, we obtain that the value of plasma temperature, averaged over space and time, is approximately equals to 2.1 keV.

This value is obviously larger than the time-averaged temperature obtained from X-ray spectroscopy measurements, since the latter corresponds to the relatively cold part of plasma torch near the ablation surface. Now, taking the average velocity of fast ions as $(E_h = m_p)^{1/2}$ (where the energy of fast ions was, approximately, expressed through the average energy of fast electrons E_h as ZE_h)

https://doi.org/10.1017/S0263034618000447 Published online by Cambridge University Press

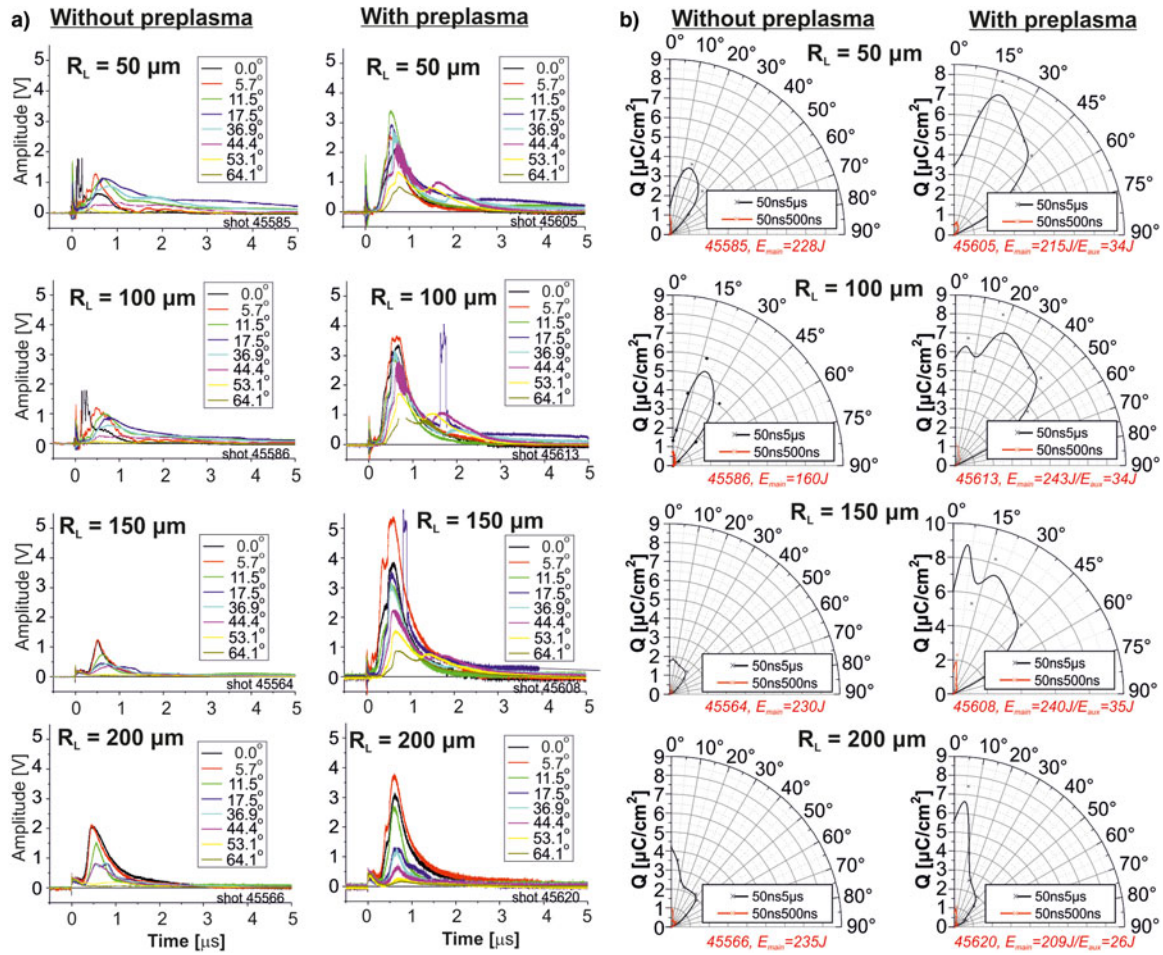

Fig. 23. Influence of the pre-plasma on: (a) the ion-collector signals measured at different angles and (b) angle distributions of the ion charge density for different focal spot radii.

and the time of the second peak as 0.15 μs, we obtain the average energy of fast electrons approximately equal to 70 keV.

Figure 23b shows the plots of charge distributions for each experimental series, calculated on the basis of integration of the charge of both thermal ions (of time-of-flight ranging in 50–500 ns).

When comparing the results from the two columns depicted in Figure 23b, it can be seen that when increasing the focal diameter, the ions are better collimated which is manifested in a distinct plasma "jet". When the pre-pulse configuration is applied together with the 200 μm focus diameter, the jet is well visible and the whole group of the pre-pulse series has considerably larger integrated charges than those obtained without the pre-pulse.

Ion emission. 3ω-experiments

The ion diagnostics applied in the PALS experiment consisted of several ion collectors installed at different angles (from 0 to 60°) at the distance of 40 cm from the target. The collected ion current was emitted from two-layer targets (see Fig. 1a). Some of the selected results provided by this diagnostic system are presented in Figure 24a and 24b.

In the left column there are the results obtained without application of pre-pulse and in the right column – those obtained with it. The parameters of the 3ω laser beam were at the same level for all the presented measurements (about 200 J in the main beam and about 40 J in the pre-pulse). Figure 24a shows the ion-collector signals for different angles and focal spot radii. All the signals for the case of both pre-plasma absence and presence correspond to thermal ions only and do not contain any response related to fast ions. It is in contrast to the results of our previous experiments carried out with the 1ω main beam, where strong signals related to fast ions were measured for the case of pre-plasma absence at high main beam intensities of $0.5–2 \times 10^{16}$ W/cm^2 (Pisarczyk *et al.*, 2015).

It should be also noted that in the case of the 1ω beam the collector signals referring to thermal ions were more than two times less compared with the 3ω-experiment for both the cases of pre-plasma absence and presence. It means that in the case of 3ω beam the absorption of laser light is significantly higher than that for the 1ω beam. According to the results of numerical simulations presented in the next paragraph, the absorption efficiency for 3ω is 0.7–0.8, while for 1ω (Pisarczyk *et al.*, 2015) it was 0.4–0.5. Other conclusions deduced from the ion-collector measurements (Fig. 24a) may be summarized as below:

- The number of thermal ions in the case of pre-plasma presence is approximately 1.2–1.5 times larger than that observed in the case of pre-plasma absence for all the focal spot radii.
- The signal of fast ions is not measurable, which confirms the results of previous paragraphs concerning the negligible effect of fast electron generation.

https://doi.org/10.1017/S0263034618000447 Published online by Cambridge University Press

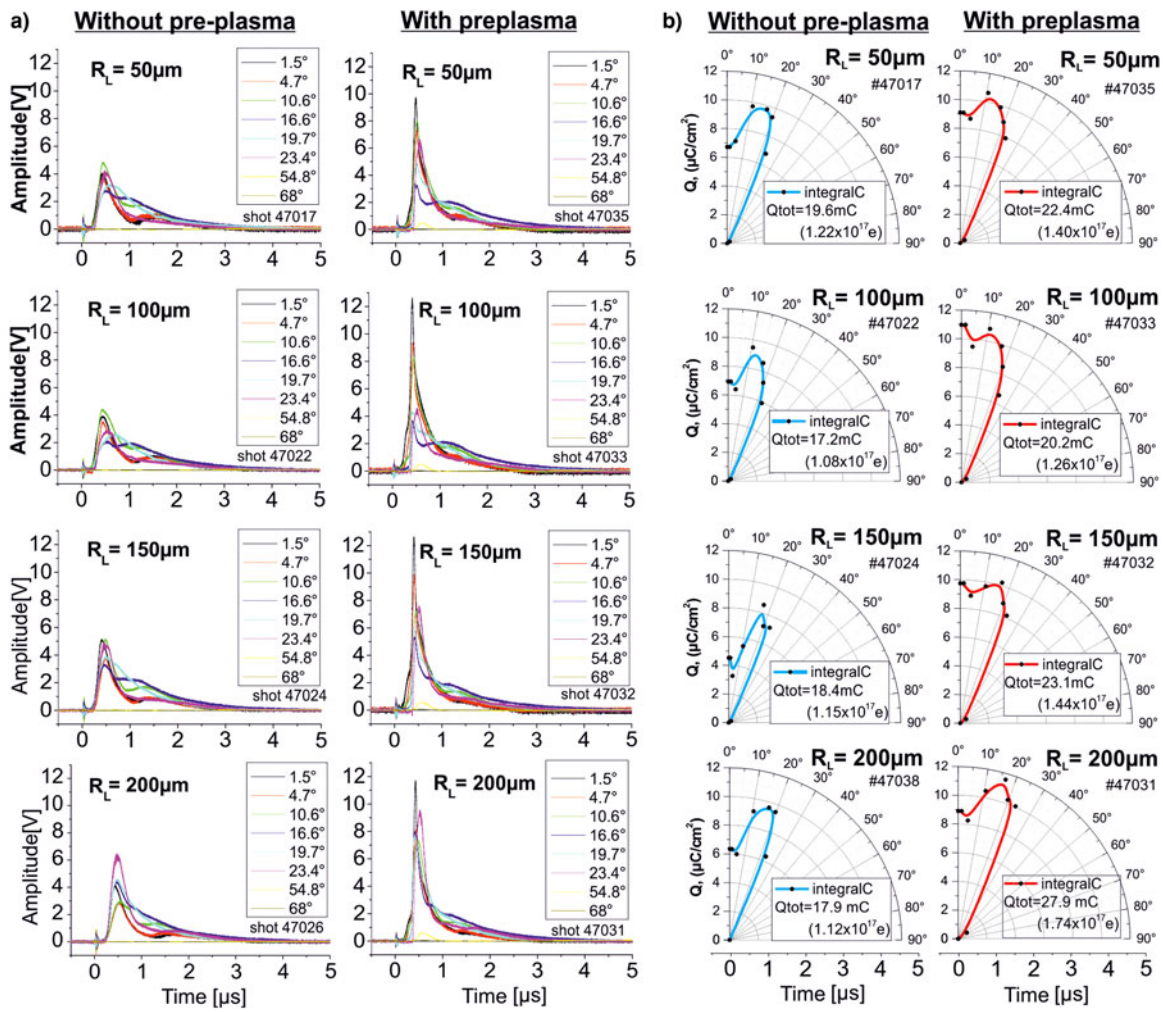

Fig. 24. Influence of the pre-plasma on: (a) the ion-collector signals measured at different angles and (b) angle distributions of the ion charge density for different focal spot radii.

- Thermal ion signals peak practically at the same time for both the cases of pre-plasma presence and absence, at about 0.5 μs, which is smaller by a factor of 1.4–1.6 in comparison with the case of 1ω main pulse (Pisarczyk *et al.*, 2015). It means that the temperature of plasma produced by 3ω beam is higher than that generated by the 1ω beam. This correlates well with the increase of absorption efficiency for the shorter wavelengths revealed by numerical simulations.
- The ion-collector data, not separated with respect to the ion type, give a possibility to determine only the scales of temperature of the plasma plume and average energy of fast electrons. Taking the time of the second peak as 0.5 μs, the average velocity of thermal ions as $(3T/2m_p)^{1/2}$ (in the $A/Z = 2$ approximation) and the distance between target and collector equals to 40 cm, we obtain that the value of plasma temperature, averaged in space and time, is approximately equal to 3–4 keV.

Figure 24b shows the plots of charge distributions for each experimental series, calculated on the basis of integration of the charge of thermal ions (for the time-of-flight ranging from 50 to 500 ns). It can be seen that in the case of the pre-plasma presence, the ion charge density on the axis is higher compared with the case when the pre-plasma is absent.

2D numerical modeling of laser–plasma interaction in different wavelength experiments

1ω laser beam interaction

To obtain more information about the ablative plasma expansion and the fast electrons emission, the 2D-simulations were carried out using the 2D hydrodynamic code ATLANT-HE (Lebo *et al.*, 2004) from Lebedev Physical Institute in Moscow. 2D numerical code allows modeling of the following processes: the laser radiation refraction in the plasma, inverse bremsstrahlung and resonance absorption of laser radiation, generation of fast electrons due to the resonance absorption, and the fast electron energy transfer *via* Coulomb collisions. The aim of the numerical calculations was to obtain information about:

- the temporal evolution of 2D spatial distributions of the electron density as well as electron temperature of the ablation plasma;
- the fractions of the laser energy absorbed in the plasma by resonant and inverse bremsstrahlung mechanisms as well as
- the energy of fast electrons.

The calculation details are explained in our recent paper (Gus'kov *et al.*, 2014). To model the experimental conditions, the

https://doi.org/10.1017/S0263034618000447 Published online by Cambridge University Press

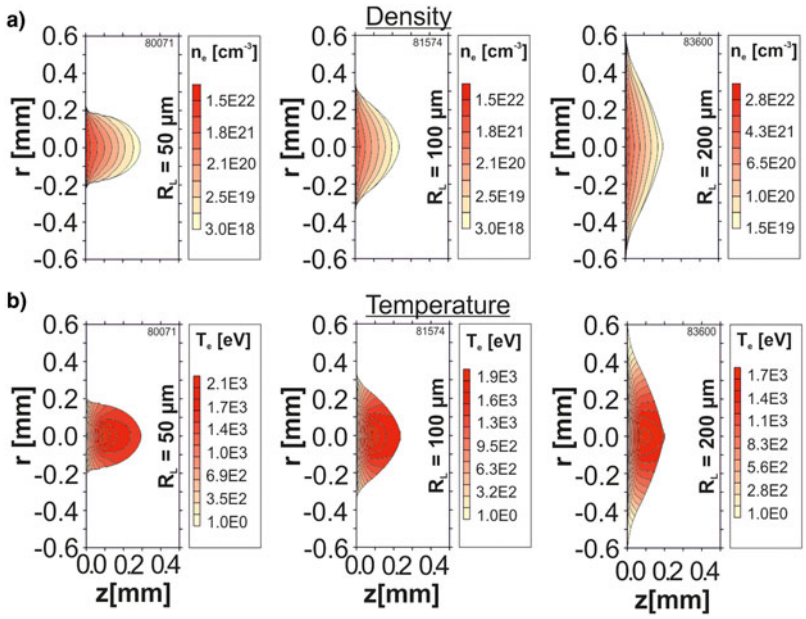

Fig. 25. The density (a) and temperature (b) distributions in the ablative plasma created by the main laser beam at the maximum of the laser pulse intensity.

computations were performed for the 1ω radiation of the main laser beam with the energy of 250 J and three values of the focal spot radius: 50, 100, and 200 µm.

In the case of a two-beam experiment referring to the SI concept, the pre-plasma was created by the auxiliary 1ω laser beam with the energy of 40 J focused on the focal spot radius R_L = 300 µm and preceding by 1.2 ns the main laser pulse. For the case of pre-plasma absence, the 2D calculations of the density and temperature corresponding to the maximum laser intensity are presented in Figure 25. In contrast to the experimental results shown in Figure 3, these density distributions do not show any growth of the axial character of plasma expansion with the increasing focal spot radii.

As demonstrated in Figure 25, the growth of the focal spot radius leads to the increased transverse dimension of the ablative plasma. The distribution of the electron density and temperature of the pre-plasma produced by the auxiliary laser beam is shown in Figure 26.

This distribution corresponds to time t = 400 ps, that is, to the end of the pulse. 2D distributions of the density and temperature characterizing the process of the interaction of the main beam with the pre-plasma created by the auxiliary laser beam are presented in Figure 27.

Compared with the situation when the pre-plasma is not created, the density scalelength of the ablative plasma is considerably larger. Comparison of the experimental data with the 2DS is presented in Table 1. This comparison has been performed in the range of the electron density smaller than 10^{20}/cm^3 as determined from the femtosecond interferometry. Table 1 indicates that there is a satisfactory agreement between experimental and numerical data in the case of pre-plasma presence. In the case of pre-plasma absence, the qualitative character is the same, but the observed and simulate the scalelength values differ considerably. The large values of experimental scalelengths result from the action of the temporally extended beam profile which is characteristic for the PALS laser and contributes to the creation of the low density plasma even in the case of pre-pulse absence.

A long pedestal (even about 1 ns long) of the pulse is not taken into account in numerical simulations. In the case of pre-plasma

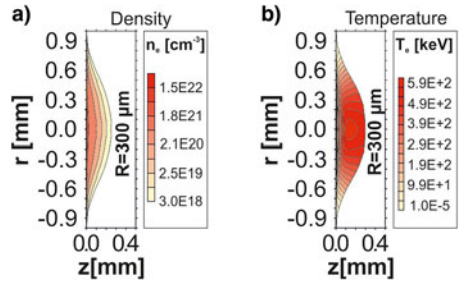

Fig. 26. Distributions of the density (a) and temperature (b) in pre-plasma for the expansion moment of t = 400 ps.

presence, the contribution of the pre-pulse is significantly smaller compared with the pre-plasma itself. This is why the experimental and numerical scalelengths agree well in the case of the pre-plasma presence. In Table 2 the numerical simulations of the total (δ_{total}), the resonant (δ_{res}) and the inverse bremsstrahlung δ_{ib} absorption coefficients are compared for the cases of the pre-plasma absence and presence.

This comparison demonstrates the significantly larger total absorption coefficient in the case of pre-plasma presence compared with the case of the pre-plasma absence. The excess is, approximately, of the factor of 3 for the beam radius of 50 µm and the factor of 2 for the beam radius of 100 µm. This explains the ion-collector measurements, where the number of thermal ions in the case of pre-plasma presence is by a factor of 2–3 larger in comparison with the case of pre-plasma absence. The maximal temperature (occurring near the region of the plasma critical density) obtained by numerical simulations falls within the interval of 2–3 keV which agrees well with the evaluation based on ion-collector data. The pre-plasma provides better conditions for resonant absorption of the laser energy. For the beam radius of 50–100 µm, the resonant absorption coefficient is equal to δ_{res} = 0.32–0.23 in the case of pre-plasma presence and to δ_{res} = 0.06–0.09 in the case of pre-plasma absence. The maximal energies of fast electrons are about 140–120 keV. This value relates to the electrons

https://doi.org/10.1017/S0263034618000447 Published online by Cambridge University Press

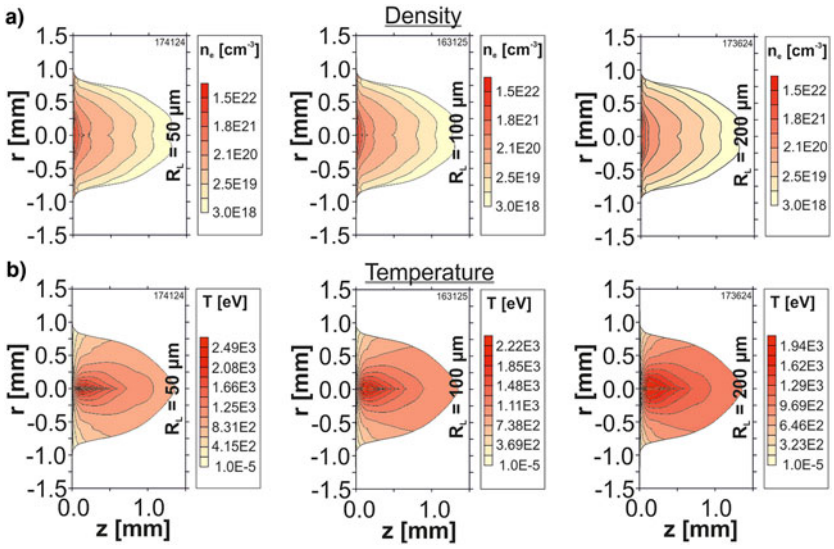

Fig. 27. The density (a) and temperature (b) distributions after the time delay of $t = 1.2$ ns relate to the auxiliary laser pulse, created when affecting the main laser beam with a pre-plasma.

Table 1. Comparison of the experimental L with the 2DS in the cases of presence and absence of pre-plasma

R_L (μm)	L (μm)			
	1ω		1ω + 1ω	
	Exp.	2D	Exp.	2D
50	125	30	326	320
100	190	36	420	346
200	140	34	365	296

which two times crossed the region of plasma resonance after their reflection from external plasma boundary.

These estimates are very close to the values evaluated from the ion-collector data. This evaluation gives the value of 70 keV of the average fast electron energy, that corresponds to the maximal energy of 140 keV. According to the numerical modeling presented in Gus'kov *et al.* (2014), the increased efficiency of the resonance absorption in the case of pre-plasma results probably from a better fitting of the angles between the individual laser beams and the direction of the density gradient near the critical surface (these angles are closer to optimum angles because of a smaller scalelength).

3ω laser beam interaction

2DSs of the ablative plasma created by the 3ω main laser beam were carried out using the 2D hydrodynamic code ATLANT-HE, which was described in section "1ω laser beam interaction". Analogously as in the 1ω experiment to compare the experimental results obtained by femtosecond interferometry and fast electron measurements with 2DSs was the main task, in order to formulate final conclusions about the laser energy transport to the shock wave with the participation of fast electrons.

To model the experimental conditions, the computations were performed for the 3ω radiation of the main laser beam with the energy of 200 J and three values of the focal spot radius: 50, 100, and 200 μm. In the case of two-beam experiment, the pre-plasma was created by an auxiliary 1ω laser beam of energy of 40 J, focused on a focal spot radius R_L of 300 μm and preceding the main laser pulse by 1.2 ns.

For the case of pre-plasma absence, the 2D calculations of the density and temperature show that the increase of focal spot radius leads to an increase of transverse size and a decrease of axial size of expanding plasma. Due to that, the angles between the directions of density gradient and the normal to the target surface decrease and the geometry of expansion is close to a planar one. Similarly as for the 1ω-experiments (without pre-plasma), the 2D calculations of the density and temperature do not show any growth of the axial character of plasma expansion with the increasing focal spot radii (Pisarczyk *et al.*, 2015).

A satisfactory agreement of calculations with the experiment was obtained in the case of laser beam interaction with a two-layer target (Fig. 1) in the presence of pre-plasma. A comparison of the axial density profiles and L in the ablative plasma, in the cases of both pre-plasma absence and presence, is presented in Figure 28. As it results from Figure 28, the scalelength of the ablative plasma in the case of the pre-plasma presence is considerably larger in comparison with the situation when the pre-plasma is not created.

A more detailed comparison of the experimental data with the 2DS is presented in Tables 3 and 4. As in the 1ω-experiments presented in the previous chapter, the comparison of the experimental and simulation data has been performed in the range of the electron density smaller than $10^{20}/cm^3$. Table 3 shows a satisfactory agreement between experimental and numerical data in the case of pre-plasma presence. In the case of pre-plasma absence, the qualitative character is the same but the observed and simulated L values differ considerably. The large values of experimental L result from the action of the temporarily extended beam profile which is characteristic for the PALS laser and contributes to creation of a low density plasma even in the case of pre-pulse absence. It was explained in the previous section.

In Table 4 the numerical simulations of the total (δ_{total}), resonant (δ_{res}), and inverse bremsstrahlung (δ_{ib}) absorption coefficients are compared for the cases of pre-plasma absence and presence.

From Table 4 it results that in the case of absence of pre-plasma, the total absorption increases with the increasing focal spot radius from 0.593 to 0.876. In contrast, the fraction of resonant absorption decreases from 0.0883 to 0.0697 staying small.

https://doi.org/10.1017/S0263034618000447 Published online by Cambridge University Press

Table 2. Comparison of numerical simulations of the total δ_{total}, resonant δ_{res}, and inverse bremsstrahlung δ_{ib} absorption coefficients in the cases of pre-plasma absence and presence

R_L (μm)	50 1ω	1ω + 1ω	100 1ω	1ω + 1ω	200 1ω	1ω + 1ω
δ_{total}	0.21	0.64	0.29	0.57	0.42	0.59
δ_{ib}	0.15	0.31	0.19	0.34	0.25	0.39
δ_{res}	0.06	0.32	0.09	0.23	0.17	0.21
$E_{h(max)}$ (keV)	143	152.8	129	144	121	114
T_{emax} (keV)	2.48	3.27	2.20	2.99	1.92	2.31

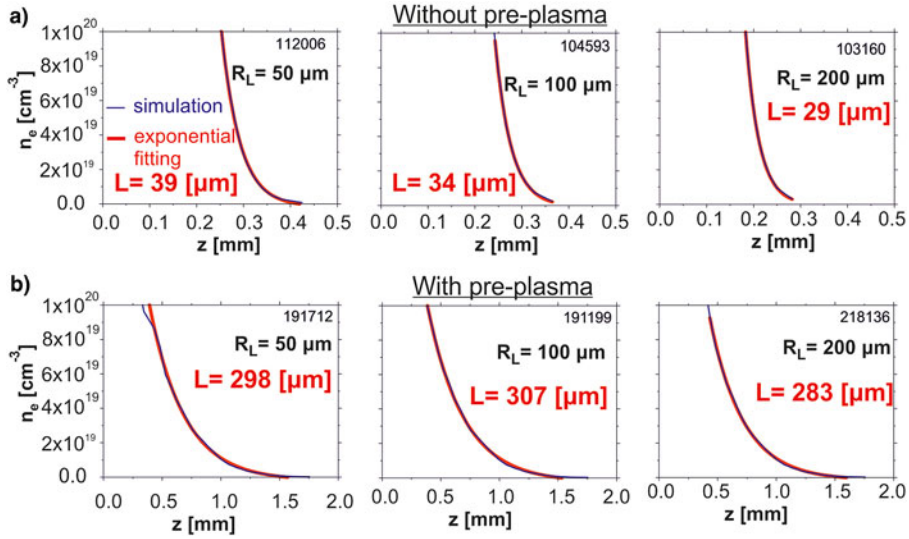

Fig. 28. Comparison of the axial density profiles and the scale-length obtained in the cases of: (a) absence and (b) presence of pre-plasma.

Table 3. Comparison of the experimental values L with the 2DS in the cases of presence and absence of pre-plasma

R_L (μm)	L (μm)			
	3ω		1ω + 3ω	
	Exp.	2D	Exp.	2D
50	125	39	220	298
100	115	34	290	307
200	100	29	340	283

The average energy of fast electrons $E_{h(max)}/2$ is about 30–35 keV for both the cases with and without pre-plasma. The average fast electron energy is close to the experimental values obtained from Cu K_α line measurements in the experiment without a pre-plasma. The pre-pulse has a small effect on these quantities and does not alter their dependence on the radius of the main beam. These results differ significantly from the case of the 1ω main pulse which was presented in section "1ω laser beam interaction" [see Table 2 and the paper of Pisarczyk *et al.*, (2015)].

Numerical simulations show that without pre-plasma, the total absorption is considerably larger for 3ω than that of the 1ω main pulse. This is confirmed by the data from ion-collector measurements. The fraction of the resonance absorption is about the same. The pre-plasma has a small effect on absorption in the 3ω case and strong effect in the case of 1ω. In the case with pre-plasma, for the 3ω main pulse the fraction of resonance absorption (and hence the energy contained in the fast electrons) is several times smaller than that for the 1ω main pulse. This is confirmed by ion-collector measurements, too. The average energy of fast electrons generated by resonant absorption is approximately two times smaller in the case of the 3ω main pulse (30–35 keV) as compared with the 1ω main pulse (50–70 keV) (Pisarczyk *et al.*, 2015).

Conclusion

1ω-experiment

Summing up the comparison of the experimental and numerical data we can claim that:

- Based on the interferometric results, measurements of the crater volume, spectroscopic determination of the temperature, and density near the ablation surface, and imaging *via* K_α emission, there is a good reason to conclude that the presence of pre-plasma leads to a decrease in the energy transfer efficiency of the main 1ω laser beam to a solid target by means of fast electrons. In the same time, 2DSs show that the presence of pre-plasma makes the conditions of resonant absorption of the laser radiation more favorable, increases the fraction of the laser energy absorbed by resonant mechanism, and hence increases the energy contained in the fast electron stream.

https://doi.org/10.1017/S0263034618000447 Published online by Cambridge University Press

Table 4. Comparison of numerical simulations of the total δ_{total}, resonant δ_{res}, and inverse bremsstrahlung δ_{ib} absorption coefficients in the cases of pre-plasma absence and presence

R_L (μm)	50		100		200	
	3ω	1ω + 3ω	3ω	1ω + 3ω	3ω	1ω + 3ω
δ_{total}	0.593	0.553	0.751	0.691	0.876	0.789
δ_{ib}	0.505	0.462	0.655	0.592	0.806	0.716
δ_{res}	0.0883	0.091	0.0963	0.0993	0.0697	0.0733
$E_{h(max)}$ (keV)	69.4	73.8	62.3	69.6	58.2	54.8
T_{emax} (keV)	3.67	3.91	2.81	3.27	2.09	2.58

- The results of the interferometric measurements, as well as the results of 2DSs, show that the presence of pre-plasma decreases the axial density gradient.
- The decrease of the contribution of the fast electron energy transfer to a solid target when increasing the laser energy converted to fast electrons can be explained by the deterioration of the conditions of energy transfer by fast electrons in the presence of pre-plasma. There are two reasons for such a decline:
  - a large divergence of streaming fast electrons which are generated far from the target surface in the presence of pre-plasma and
  - the effect of plasma density gradient at the irradiated target boundary on the efficiency of energy transfer from the streaming fast electrons to the shock wave. Such an effect was predicted and numerically investigated in Nicolai *et al.* (2014).

3ω-experiment

The performed investigations show that by using the third-harmonic main pulse the laser energy conversion into the energy of fast electrons is very small – the fraction of fast electron energy does not exceed a few tenths of a percent of laser energy both in the absence and in the presence of pre-plasma. This conclusion deduced from K_α-emission measurements and numerical simulations is confirmed by the measurements of ion yield and volumes of laser-produced craters, which characterizes the amount of energy transferred to shock waves. The measurements of ion signals show virtually no contribution of the fast ion component. The crater volume measurements, in combination with femtosecond interferometry, both in the cases of pre-plasma presence and absence, show that the target ablation and evolution of laser-produced plasma are determined by energy transfer *via* electron conductivity under conditions of 1D or 2D matter expansion without any appreciable effect of energy transfer by fast electrons. Both the maximal volume of the crater (the maximum energy of the shock wave) and the minimal N/V_{cr} parameter corresponds to the greatest radius of the focal spot at which the negative effect of 2D-expansion of plasma is minimal and, as a result, the ablation pressure is maximal (Gus'kov *et al.*, 2004, 2014). This result holds for the experiments both in absence and presence of pre-plasma. With the decrease of focal spot radius the negative effect of 2D-plasma expansion increases and the crater volume decreases. This is in contrast with experiments with the first-harmonic main pulse, in which increasing the intensity of long-wavelength radiation leads to such a significant generation of fast electrons by the resonance mechanism and to such a strong effect of the fast electron energy transfer in the target depth that its contribution to the shock generation is significant and the crater volume strongly increases with decreasing the focal spot radius (Gus'kov *et al.*, 2004, 2006, 2014).

Acknowledgements. This work has been carried out within the framework of the EUROfusion Enabling Research Project: AWP17-ENR-IFE-CEA-01 "Preparation and Realization of European Shock Ignition Experiments" and has received funding from the Euratom research and training programme 2014–2018 under grant agreement no. 633053. The views and opinions expressed herein do not necessarily reflect those of the European Commission. The work was also supported by the European Union LASERLAB IV project (Grant Agreement No. 654148), by the Russian Foundation for Basic Research under the Project No. 17-02-00059, by the MEPhI Academic Excellence Project (contract no. 02.a03.21.0005, 27.08.2013), by the Czech Ministry of Education, Youth and Sports, project LD14089 and projects LM2010014 and LM2015083 (PALS RI), and by the Czech Science Foundation, Project No. P205/11/P712. The authors also acknowledge support from the project High Field Initiative (HiFI) (CZ.02.1.01/0.0/0.0/15 003/0000449) and ELI Tools for Advanced Simulation (ELITAS) (CZ.02.1.01/0.0/0.0/16013/0001793), both from European Regional Development Fund. Finally, the authors are grateful to the PALS staff for help in running the experiments.

Author ORCIDs. Tadeusz Pisarczyk http://orcid.org/0000-0002-1109-7683.

References

Batani D, Antonelli L, Atzeni S, Badziak J, Baffigi F, Chodukowski T, Consoli F, Cristoforetti G, De Angelis R, Dudzak R, Folpini G, Giuffrida L, Gizzi LA, Kalinowska Z, Koester P, Krousky E, Krus M, Labate L, Levato T, Maheut Y, Malka G, Margarone D, Marocchino A, Nejdl J, Nicolai P, O'Dell T, Pisarczyk T, Renner O, Rhee YJ, Ribeyre X, Richetta M, Rosinski M, Sawicka M, Schiavi A, Skala J, Smid M, Spindloe C, Ullschmied J, Velyhan A and Vinci T (2014) Generation of high pressure shocks relevant to the shock-ignition intensity regime. *Physics of Plasmas* **21**, 032710.

Borodziuk S, Kasperczuk A, Pisarczyk T, Gus'kov SYu, Ullschmied J, Kralikova B, Rohlena K, Skala J, Kalal M and Pisarczyk P (2004*a*) Investigation of plasma ablation and crater formation processes in the Prague Asterix Laser System laser facility. *Optica Applicata* **34**, 31–42.

Borodziuk S, Kasperczuk A, Pisarczyk T, Demchenko NN, Guskov SYu, Rozanov VB, Kalal M, Limpouch J, Ullschmied J, Kondrashov VN and Pisarczyk P (2004*b*) Application of the 3-frame interferometry and the crater replica method for investigation of laser accelerated macroparticles interacting with massive targets in the pals experiment. *Optica Applicata* **34**, 385–403.

Borodziuk S, Demchenko NN, Gus'kov SYu, Jungwirth K, Kalal M, Kasperczuk A, Kondrashov VN, Krousky E, Limpouch J, Masek K, Pisarczyk P, Pisarczyk T, Pfeifer M, Rohlena K, Rozanov VB, Skala J and Ullschmied J (2005) High power laser interaction with single and double layer targets. *Optica Applicata* **35**, 242–262.

Dostal J, Dudzak R, Pisarczyk T, Pfeifer M, Huynh J, Chodukowski T, Kalinowska Z, Krousky E, Skala J, Hrebicek J, Medrik T, Golasowski J,

https://doi.org/10.1017/S0263034618000447 Published online by Cambridge University Press

Juha L and Ullschmied J (2017) Synchronizing single-shot high-energy iodine photodissociation laser PALS and high-repetition-rate femtosecond Ti:sapphire laser system. *Review of Scientific Instruments* **88**, 045109.

Gus'kov SYu, Borodziuk S, Kalal M, Kasperczuk A, Kralikova B, Krousky E, Limpouch J, Masek K, Pisarczyk P, Pisarczyk T, Pfeifer M, Rohlena K, Skala J and Ullschmied J (2004) Shock wave generation and crater formation in solids by a short laser pulse interaction. Generation of shock waves and formation of crater in a solid material irradiated by a short laser pulse. *Quantum Electronics* **34**, 989–1003.

Gus'kov SYu, Kasperczuk A, Pisarczyk T, Borodziuk S, Kalal M, Limpouch J, Ullschmied J, Krousky E, Masek K, Pfeifer M, Rohlena K, Skala J and Pisarczyk P (2006) Efficiency of ablative loading of material upon the fast-electron transfer of absorbed laser energy. *Quantum Electronics* **36**, 429–434.

Gus'kov SYu, Demchenko NN, Kasperczuk A, Pisarczyk T, Kalinowska Z, Chodukowski T, Renner O, Smid M, Krousky E, Pfeifer M, Skala J, Ullschmied J and Pisarczyk P (2014) Laser-driven ablation through fast electrons in pals experiment at the laser radiation intensity of 1–50 PW/cm^2. *Laser and Particle Beams* **32**, 177–195.

Kalinowska Z, Kasperczuk A, Pisarczyk T, Chodukowski T, Gus'kov SYu, Demchenko NN, Ullschmied J, Krousky E, Pfeifer M, Rohlena K, Skala J and Pisarczyk P (2012) Investigations of mechanisms of laser radiation absorption at PALS. *Nukleonika* **57**, 227–230.

Kasperczuk A, Makowski J, Paduch M, Tomaszewski K, Wereszczynski Z, Wolowski J and Wyzgal J (1993) Application of fast three-frame interferometry to investigation of laser plasma. *Proceedings of SPIE* **2202**, 449.

Koester P, Antonelli L, Atzeni S, Badziak J, Baffigi F, Batani D, Cecchetti CA, Chodukowski T, Consoli F, Cristoforetti G, De Angelis R, Folpini G, Gizzi LA, Kalinowska Z, Krousky E, Kucharik M, Labate L, Levato T, Liska R, Malka G, Maheut Y, Marocchino A, O'Dell T, Parys P, Pisarczyk T, Raczka P, Renner O, Rhee YJ, Ribeyre X, Richetta M, Rosinski M, Ryc L, Skala J, Schiavi A, Schurtz G, Smid M, Spindloe C, Ullschmied J, Wolowski J and Zaras A (2013) Recent results from experimental studies on laser–plasma coupling in a shock ignition relevant regime. *Plasma Physics and Controlled Fusion* **55**, 124045.

Lebo IG, Demchenko NN, Iskakov AB, Limpouch J, Rozanov VB and Tishkin VF (2004) Simulation of high-intensity laser plasma interactions by use of the 2D Lagrangian code ATLANT-HE. *Laser and Particle Beams* **22**, 267–273.

Nicolai PH, Feugeas JL, Toutati M, Ribeyre X, Gus'kov SYu and Tikhonchuk V (2014) Deleterious effects of nonthermal electrons in shock ignition concept. *Physical Review E* **89**, 033107.

Pisarczyk T, Gus'kov SYu, Kalinowska Z, Badziak J, Batani D, Antonelli L, Folpini G, Maheut Y, Baffigi F, Borodziuk S, Chodukowski T, Cristoforetti G, Demchenko NN, Gizzi LA, Kasperczuk A, Koester P, Krousky E, Labate L, Parys P, Pfeifer M, Renner O, Smid M, Rosinski M, Skala J, Dudzak R, Ullschmied J and Pisarczyk P (2014) Pre-plasma effect on energy transfer from laser beam to shock wave generated in solid target. *Physics of Plasmas* **21**, 012708.

Pisarczyk T, Gus'kov SYu, Renner O, Demchenko NN, Kalinowska Z, Chodukowski T, Rosinski M, Parys P, Smid M, Dostal J, Badziak J, Batani D, Volpe L, Krousky E, Dudzak R, Ullschmied J, Turcicova H, Hrebicek J, Medrik T, Pfeifer M, Skala J, Zaras-Szydlowska A, Antonelli L, Maheut Y, Borodziuk S, Kasperczuk A and Pisarczyk P (2015) Pre-plasma effect on laser beam energy transfer to a dense target under conditions relevant to shock ignition. *Laser and Particle Beams* **33**, 221–236.

Pisarczyk T, Gus'kov SYu, Renner O, Dudzak R, Dostal J, Demchenko NN, Smid M, Chodukowski T, Kalinowska Z, Rosinski M, Parys P, Badziak J, Batani D, Borodziuk S, Gizzi LA, Krousky E, Maheut Y, Cristoforetti G, Antonelli L, Koester P, Baffigi F, Ullschmied J, Hrebicek J, Medrik T, Pfeifer M, Skala J and Pisarczyk P (2016) Short wavelength experiments on laser pulse interaction with extended pre-plasma at the pals-installation. *Laser and Particle Beams* **34**, 94–108.

Renner O, Smid M, Batani D and Antonelli L (2016) Suprathermal electron production in laser-irradiated Cu targets characterized by combined methods of X-ray imaging and spectroscopy. *Plasma Physics and Controlled Fusion* **58**, 075007.

Salvat F, Fernandez-Varea JM and Sempau J (2009) Penelope-2008: *A code system for Monte Carlo simulation of electron and photon transport. Workshop Proceedings* – Barcelona Spain June-3 July 2008, ISBN 978-92-64-99066-1.

Smid M, Antonelli L and Renner O (2013) X-ray spectroscopic characterization of shock-ignition-relevant plasmas. *Acta Polytechnica* **53**, 233.

https://doi.org/10.1017/S0263034618000447 Published online by Cambridge University Press